

Visualizing nuclear pore complex plasticity with Pan-Expansion Microscopy

Kimberly J. Morgan¹, Emma Carley¹, Alyssa N. Coyne^{2, 3}, Jeffrey D. Rothstein^{2, 3}, C. Patrick Lusk^{*1}, Megan C. King^{*1, 4}

¹Department of Cell Biology, Yale School of Medicine, New Haven, CT, 06520, USA.

²Brain Science Institute, Johns Hopkins University School of Medicine, Baltimore, MD, 21205, USA.

³Department of Neurology, Johns Hopkins University, Baltimore, MD, 21205, USA.

⁴Department of Molecular, Cell and Developmental Biology, Yale University, New Haven, CT, 06520, USA.

*Correspondence:

patrick.lusk@yale.edu

megan.king@yale.edu

1 **Abstract**

2

3 Cell-type specific and environmentally-responsive plasticity in nuclear pore complex
4 (NPC) composition and structure is an emerging area of investigation, but its
5 molecular underpinnings remain ill defined. To understand the cause and
6 consequence of NPC plasticity requires technologies to visualize differences within
7 individual NPCs across the thousands in a given nucleus. We evaluate the utility of
8 Pan Expansion Microscopy (Pan-ExM), which enables 16-20 fold isotropic cell
9 enlargement while preserving the proteome, to reveal NPC plasticity. NPCs are
10 robustly identified by deep learning-facilitated segmentation as tripartite structures
11 corresponding to the nucleoplasmic ring, inner ring with central transport channel,
12 and cytoplasmic ring, as confirmed by immunostaining. We demonstrate a range of
13 NPC diameters with a bias for dilated NPCs at the basal nuclear surface, often in
14 local clusters. These diameter biases are eliminated by disrupting linker of
15 nucleoskeleton and cytoskeleton (LINC) complex-dependent connections between
16 the nuclear envelope (NE) and the cytoskeleton, supporting that they reflect local
17 variations in NE tension. Pan-ExM further reveals that the transmembrane
18 nucleoporin/nup POM121 resides specifically at the nuclear ring in multiple model
19 cell lines, surprising given the expectation that it would be a component of the inner
20 ring like other transmembrane nups. Remarkably, however, POM121 shifts from the
21 nuclear ring to the inner ring specifically in aged induced pluripotent stem cell
22 derived neurons (iPSNs) from a patient with *C9orf72* amyotrophic lateral sclerosis
23 (ALS). Thus, Pan-ExM allows the visualization of changes in NPC architecture that
24 may underlie early steps in an ALS pathomechanism. Taken together, Pan-ExM is a
25 powerful and accessible tool to visualize NPC plasticity in physiological and
26 pathological contexts at single NPC resolution.

27

1 Introduction

2 The nuclear envelope (NE) is a double membrane barrier that segregates the
3 nuclear genome from the cytoplasm. Bidirectional molecular communication across
4 the NE is mediated by nuclear pore complexes (NPCs), protein gateways that
5 facilitate the selective transport of cargo-bound nuclear transport receptors (NTRs)
6 while also imposing a size-restrictive diffusion barrier. It is well understood how the
7 majority of the key building blocks (nucleoporins or nups) are arranged to build the
8 iconic 8-fold radial architecture of the NPC with recent cryo-EM and cryo-ET
9 structures approaching atomic resolution (Akey et al., 2023; Akey et al., 2022; Bley
10 et al., 2022; Fontana et al., 2022; Huang et al., 2022a; Huang et al., 2022b; Kosinski
11 et al., 2016; Mosalaganti et al., 2022; Petrovic et al., 2022; Schuller et al., 2021;
12 Singh et al., 2024; von Appen et al., 2015; Zhu et al., 2022). These studies have
13 provided a blueprint for the NPC in multiple organisms, glimpses of its evolutionary
14 history and key insights into its assembly and function. They have also revealed that
15 the NPC structure is not monolithic. Indeed, there are numerous hints that NPCs are
16 surprisingly plastic in composition and structure, but the causes and consequences
17 of this likely plasticity are just beginning to come to light (Fernandez-Martinez and
18 Rout, 2021). A key challenge for the field is to be able to directly visualize this
19 plasticity on a single NPC level.

20

21 The recent discoveries that the NPC scaffold is dilated *in cellulo* compared to in
22 isolated NEs and can constrict in response to energy depletion or hyperosmotic
23 shock suggest that lateral strain on NPCs imposed by NE tension could modulate
24 NPC architecture and function (Akey et al., 2022; Mosalaganti et al., 2022; Schuller
25 et al., 2021; Zimmerli et al., 2021). It remains unknown, however, whether changing
26 the diameter of NPCs impacts their selective permeability (although there is
27 emerging evidence that supports this concept)(Elosegui-Artola et al., 2017; Feng et
28 al., 2024; Klughammer et al., 2024; Kozai et al., 2023). Further, it is unclear whether
29 NPC diameter is controlled by passive mechanisms or whether it can be actively
30 modulated, perhaps even in response to the local NE environment. Considering the
31 latter, it is plausible that mechanotransduction mechanisms that translate
32 extracellular mechanical cues to the NE through Linker of Nucleoskeleton and
33 Cytoskeleton (LINC) complexes may locally alter NE tension and NPC dilation.
34 Consistent with this possibility, there is evidence that mechanical strain on the

1 nuclear lamina is higher at the basal versus apical surface of the nucleus (Carley et
2 al., 2021; Ihalainen et al., 2015). Whether this asymmetry in lamina tension is
3 reflected in the dilatory state of NPCs is unknown. Answering these questions will
4 require facile and accessible methods to examine NPC diameter, ideally at single
5 NPC resolution, in multiple cell types and tissues.

6
7 Similar methods are also required to tackle the question of whether NPCs are
8 compositionally (and functionally) different among cell types in both physiological
9 and pathological settings (Cho and Hetzer, 2020; Fernandez-Martinez and Rout,
10 2021). For example, it has been reported that there are at least two forms of NPCs in
11 budding yeast with either one or two nuclear rings (Akey et al., 2022). Moreover, the
12 nuclear basket is absent from many yeast NPCs and may be assembled as part of a
13 dynamic mRNA export platform (Bensidoun et al., 2022; Galy et al., 2004; Singh et
14 al., 2024). Whether there is such plasticity of the nuclear basket in human cells
15 remains unknown, but there are many hints that there is compositional heterogeneity
16 of NPCs in certain cell types driven by differential nup expression and/or turnover
17 rates, both of which may be influenced by age and disease (Cho and Hetzer, 2020).
18 Importantly, although cryo-ET may be amenable to uncovering broad classes of NPC
19 structures in scenarios where there is a total absence of a given nup, it will be less
20 valuable in cases where there may be changes in the relative stoichiometry of nups
21 within individual NPCs.

22
23 Another motivation for developing methods to visualize compositional heterogeneity
24 at the individual NPC level is exemplified by evidence that NPCs may be
25 compromised in neurodegenerative disease (Chandra and Lusk, 2022). Specifically,
26 an amyotrophic lateral sclerosis (ALS) pathomechanism caused by a hexanucleotide
27 repeat expansion in the *C9orf72* gene has been proposed to occur through an NPC
28 injury cascade resulting in the loss of a specific subset of nups from a fraction of
29 NPCs (Coyne et al., 2020). POM121, one of three transmembrane nups, is a key
30 linchpin whose disappearance precedes that of other nups that ultimately herald a
31 loss of nuclear compartmentalization (Baskerville et al., 2024; Coyne et al., 2021).
32 The underlying mechanisms that drive these changes to NPCs remains uncertain but
33 would clearly benefit from a methodology that can reveal the molecular and
34 morphological changes that occur within individual NPCs along the NPC injury

1 cascade. Moreover, the ideal method would couple quantitative immunolabeling with
2 the capacity to assess gross changes in NPC architecture.

3

4 Here, we explore the utility of Pan Expansion Microscopy (Pan-ExM) to robustly
5 visualize the molecular composition and structure of individual NPCs. Pan-ExM is
6 unique over other expansion microscopy methods as it preserves the total proteome,
7 which can be visualized at an ultrastructural resolution using a “pan” fluorescent
8 protein stain (M'Saad and Bewersdorf, 2020). We demonstrate that machine-
9 learning based segmentation of Pan-ExM images can robustly and comprehensively
10 identify individual NPCs. Not only can Pan-ExM reveal the compositional
11 heterogeneity of NPCs on an individual NPC level but it can also reveal local
12 differences in NPC diameter tied to cell polarity that depend on LINC complexes.
13 Further, we used Pan-ExM to make the unexpected discovery that, unlike the other
14 transmembrane nups, POM121 is asymmetrically distributed to the nuclear ring.
15 Most remarkably, although POM121’s nuclear ring localization is observed across
16 several human cell lines, in induced pluripotent stem cell derived neurons (iPSNs)
17 from a patient with the pathological *C9orf72* repeat expansion, we observed a shift in
18 the distribution of POM121 from the nuclear ring to the inner ring that we tie to
19 further loss of NPC density as revealed by the pan-stain. These data suggest that
20 discrete changes to NPC architecture in the *C9orf72* ALS NPC injury cascade that
21 were previously unappreciated are visible by Pan-ExM. Thus Pan-ExM is a valuable
22 discovery tool that will help illuminate NPC plasticity – an essential step towards
23 understanding its function across cells and tissues.

24

1 **Results**

2 **Pan-ExM permits visualization of whole cell proteinaceous ultrastructure** 3 **including NPCs.**

4 To visualize cellular ultrastructure and NPCs, we leveraged the Pan ExM (M'Saad
5 and Bewersdorf, 2020) protocol and fixed and embedded samples in a series of
6 swellable hydrogels, enabling ~16-fold expansion (Supplementary Figure 1). A
7 schematic of the procedures and computational tools used in this study are
8 diagrammed in Figure 1. Briefly, to “pan” stain all cellular proteins, lysines across the
9 proteome were labeled with a fluorophore conjugated N-Hydroxysuccinimide (NHS),
10 DNA was labeled with SYTOX Green and proteins of interest were labeled with
11 antibodies (Figure 1a). Using confocal microscopy, we acquired images capturing
12 whole cell volumes. As expected (M'Saad and Bewersdorf, 2020), cellular organelles
13 like nucleoli, mitochondria, Golgi stacks and centrioles were identifiable by their
14 characteristic ultrastructural morphologies revealed by the pan-stain (Figure 1b).
15 NPCs were likewise visible at the edge of the nucleus (Figure 1b). We developed an
16 image analysis pipeline using Imaris software and the Fiji (Schindelin et al., 2012)
17 plugin LABKIT (Arzt et al., 2022), a machine-learning based random forest classifier,
18 to segment cellular structures in 3D (Figure 1c). Through manual labeling of image
19 voxels in all acquired channels, nuclei were segmented by iterative training. NPCs
20 were robustly identified in all axial orientations and automatically segmented by
21 training multiple datasets. To measure NPC diameter required training a different
22 classifier to accurately segment the nuclear ring of NPCs. This analysis was further
23 combined with segmentation of antibody labeling and annulate lamellae (AL).
24 Together, these in silico segmentation approaches enable a detailed ultrastructural
25 analysis of all NPCs in a given cell nucleus in virtually any cell line. Initially, we
26 examined three commonly used cell lines: HeLa cervical adenocarcinoma, A549
27 lung adenocarcinoma and SH-SY5Y neuroblastoma cells.

28

29 In axial sections of magnified views of the nuclear surface, each NPC (regardless of
30 cell line) was comprised of a single focus suspended between two rings (Figure 2a).
31 The former is best observed in cross section (Figure 2b). Consistent with a body of
32 prior work (Krull et al., 2010; M'Saad and Bewersdorf, 2020; Ou et al., 2017;
33 Schermelleh et al., 2008) supporting that NPCs engage euchromatin and/or exclude
34 heterochromatin, the nuclear rings were nestled within islands lacking detectable

1 SYTOX fluorescence (Figure 2a, bottom panels). A quantitative comparison of the
2 average NPC architecture derived from 2061 NPCs in Pan-ExM samples with those
3 derived from *in cellulo* cryo-ET of human NPCs (Mosalaganti et al., 2022; Schuller et
4 al., 2021) indicates that Pan-ExM results in expansion of the NPC ~2 fold more
5 along the nuclear transport axis compared to the radial axis (Supplementary Figure
6 2a). Indeed, comparing the relative dimensions observed in the expanded NPCs to
7 the average cryo-ET structure of NPCs in intact DLD-1 cell nuclei (Schuller et al.,
8 2021) supports that Pan-ExM maintains a faithful relationship between the diameter
9 of the nuclear and inner rings (Supplementary Figure 2b, c). Moreover, we can also
10 discern that the inner ring is more proximal to the nuclear ring than the cytoplasmic
11 ring, a prominent feature of the DLD-1 NPC model (Schuller et al., 2021)
12 (Supplementary Figure 2a, b, d). However, the dimensions along the nuclear
13 transport axis are exaggerated (Supplementary Figure 2a). Regardless, NPCs and
14 their substructure are easily visualized by Pan-ExM with the relative dimensions of
15 the nuclear, inner and cytoplasmic rings preserved.

16

17 The ability to segment NPCs and nuclear contours provided a facile approach to
18 automate counting all the NPCs of hundreds of HeLa, A549 and SH-SY5Y nuclei
19 and to correlate these values to nuclear surface and volume measurements. The
20 latter were normalized to an expansion factor calculated for each sample by
21 measuring the mean distance between the membranes of mitochondria cristae
22 (Supplementary Figure 1a) and centriole diameters (Supplementary Figure 1b); the
23 average of these two was then taken as the expansion factor for assigning pre-
24 expansion scale (Supplementary Figure 1c). There was remarkable consistency in
25 sample-to-sample expansion that ranged from 13.94 to 16.69 fold (Supplementary
26 Figure 1d). On average, the three cell lines had a similar mean number of NPCs with
27 considerable variability on an individual cell basis. HeLa cells displayed the largest
28 spread in values (over 7-fold) and SH-SY5Y cells, the least (Figure 2c). As such, SH-
29 SY5Y cells also had the highest density of NPCs that were closest to each other
30 (Figure 2d,e). To gain some insight into the mechanisms that may influence NPC
31 number, we further related NPC number to the nuclear surface area and nuclear
32 volume on an individual cell basis. Across all cells examined, NPC number was
33 correlated with nuclear surface area (Figure 2e-h) and nuclear volume (Figure 2i-l),

1 with modestly stronger correlations with nuclear volume. Thus, Pan-ExM is a
2 valuable and facile approach to count NPCs in relation to nuclear metrics.

3

4 **Local differences in NPC dimensions**

5 Emerging work has intimated that the NPC diameter adopts a range of dilation states
6 in response to NE tension, which in turn may be modulated by both cell-intrinsic and
7 extrinsic factors (Mosalaganti et al., 2022; Schuller et al., 2021; Zimmerli et al.,
8 2021). Although an exciting concept, we know little about the factors that govern if
9 NPCs in a single nucleus exist in different dilatory states and, if so, if this is
10 biologically meaningful. While the most pronounced quantitative changes in NPC
11 diameter when comparing a no tension state (isolated NEs) and a physiological
12 tension state (*in cellulo*) manifest at the inner ring, which expands ~30% in two
13 different cryo-ET models of human cells (Mosalaganti et al., 2022; Schuller et al.,
14 2021), changes in tension are also reflected in the pore membrane to pore
15 membrane distance (a 12-18% expansion in human cells (Mosalaganti et al., 2022;
16 Schuller et al., 2021). The effect of NE tension on the dilation of the nuclear and
17 cytoplasmic rings is more modest and most clearly revealed by comparing fission
18 yeast NPC cryo-ET structures in different NE tension states – here a 13% change in
19 the nuclear ring diameter was observed (Zimmerli et al., 2021). It is important to
20 note, however, that the cryo-ET models are all averaged structures, and the inner
21 ring diameter of individual NPCs in cryo-ET preparations varies remarkably (Schuller
22 et al., 2021; Zimmerli et al., 2021). To test whether Pan-ExM could provide a tool to
23 readily evaluate relative NPC diameter within individual cells at high sampling
24 density, we measured the diameters of thousands of nuclear rings of computationally
25 segmented NPCs on a given HeLa nucleus as this element of the NPC allowed for
26 the most robust measurements. In line with prior observations (Schuller et al., 2021),
27 we likewise noted that there was a near two-fold range in NPC diameter values
28 across the nucleus (Figure 3a). Leveraging our ability to comprehensively assess all
29 NPCs, we further investigated whether shifts in this range are likely to reflect bona
30 fide local NPC diameter differences. To that end we compared the diameters of
31 NPCs on the top and bottom of the nucleus; there is evidence that tension on the
32 nuclear lamina is higher on the bottom of the nucleus due to cell adhesion to the
33 extracellular matrix (Carley et al., 2021; Ihalainen et al., 2015). Consistent with the
34 expectation that higher force transduction to the nuclear lamina increases NE

1 tension in a way that could enhance NPC dilation, we observed a significant trend of
2 larger NPC diameters on the basal surface of the nucleus compared to the apical
3 surface, although there is a marked variance across the NPC population on both
4 surfaces (Figure 3a). This NPC diameter bias between the basal and apical aspects
5 of the nucleus was mirrored in both A549 and SH-SY5Y cells (Figure 3d;
6 Supplementary Figure 3), supporting that this is a general phenomenon. One
7 interpretation of these data is that there are localized regions of high NE tension,
8 particularly on the basal nuclear surface.

9
10 Interestingly, when we binned the NPC diameters into quintiles, the distance to the
11 five nearest NPCs in the same diameter class was shortest for NPCs with the largest
12 20% of diameters (Figure 3b). Indeed, compared to a randomly selected 20%,
13 middle 20% or to the smallest 20%, the largest NPCs were significantly closer
14 together. Color-coding of NPCs at the basal nuclear surface according to NPC
15 diameter class revealed that larger NPCs appeared to locally cluster in apparent hot
16 spots (Figure 3c, purple). These results were mirrored in A549 cells (Figure 3e, f).
17 Thus, a generalizable principle appears that the largest NPCs cluster together in
18 local regions across the nuclear surface.

19
20 To investigate whether the measured biases in NPC diameter reflected the functional
21 integration of NPCs within a mechanoresponsive network (and to rule out expansion-
22 induced artifacts), we performed Pan-ExM and measured NPC diameters in
23 CRISPR-edited A549 cells lacking *Sun1* and *Sun2* (Supplementary Figure 4). SUN1
24 and SUN2 are integral components of LINC complexes (Chang et al., 2015)
25 necessary to transmit cytoskeletal forces from cell-matrix adhesions to the nuclear
26 lamina (Carley et al., 2021). Strikingly, the ablation of LINC complexes completely
27 disrupted the observed bias for larger NPC diameters on the basal surface of the
28 nucleus (Figure 3g), which were now also found to be uniformly distributed (Figure
29 3i). Indeed, we no longer detected a bias for the largest NPCs to cluster (Figure 3h,
30 i). Thus, Pan-ExM can detect LINC-complex dependent changes in relative NPC
31 diameter within single nuclei while also providing evidence for a putative
32 mechanoresponsive response that has yet to be directly documented.

33

1 Last, the modest magnitude of the shift in the mean nuclear ring diameter at the top
2 and bottom of the nucleus in the Pan-ExM samples is in line with the expectation that
3 it is far less susceptible to tension-induced dilation than the inner ring. In addition,
4 even in the context of LINC complex ablation, there is likely remaining tension on the
5 NE driven by other mechanisms (e.g. compressive actomyosin networks or colloidal
6 osmotic pressure) that may prevent the complete relaxation of NPCs. We therefore
7 investigated the diameters of NPCs in Pan-ExM samples within annulate lamellae
8 (AL), stacks of ER sheets filled with NPCs that would not be predicted to be under
9 tension. Consistent with this idea, the NPC diameter in AL was markedly (35%)
10 reduced compared to NPCs at the NE (Figure 3a). When taken together, our findings
11 reinforce that Pan-ExM can reveal the conformation of individual NPCs and is
12 therefore an invaluable approach for detecting a range of relative NPC diameters
13 that could reflect distinct NPC states. Moreover, our observations suggest that while
14 LINC complex-dependent tension states at the NE can meaningfully influence NPC
15 diameter, this quantitative effect remains only a fraction of the variance in NPC
16 diameters that are observed even within the same nucleus.

17

18 **Nup antibody labeling defines NPC ultrastructure in Pan-ExM**

19 We next assessed whether individual nups could be localized within the Pan-ExM
20 ultrastructure by immunostaining of expanded cells with a battery of nup specific
21 antibodies. We tested antibodies directed against nups representative of all major
22 NPC architectural elements (Figure 4a, Supplementary Figure 5) including the
23 cytoplasmic and nucleoplasmic rings, the inner ring, the FG-rich central channel, the
24 nuclear basket, and the cytoplasmic filaments (Figure 4b). The anti-nup antibodies
25 specifically labeled one or more of the three substructures of the expanded NPCs in
26 a manner congruent with their established locations. For example, we observed anti-
27 NUP107 staining at both pan-stained rings confirming these to be the cytoplasmic
28 and nucleoplasmic rings (Figure 4a-c). By contrast, the pan-stained focus suspended
29 between the two rings was recognized by antibodies to the central channel FG-nups
30 NUP62 and NUP98, the inner ring component, NUP93, and the integral membrane
31 nucleoporins NDC1 and GP210. Thus, this middle focus represents the inner ring
32 with FG-network. Last, although the position of the nuclear basket (NUP50, NUP153,
33 TPR) and cytoplasmic filament (NUP358) labels also converged qualitatively on the
34 pan-stained cytoplasmic and nucleoplasmic rings, quantification of the label position

1 relative to the SYTOX stain (after normalization to the position of NUP107 to define
2 the “middle” of the NPC) supports that they do, as expected, extend away from the
3 rings into the nucleoplasm and cytoplasm, respectively (Figure 4c). Thus, the overall
4 position of nups within the NPC architecture is retained during fixation and expansion
5 of NPCs.

6

7 As the pan-stain identifies all NPCs and major architectural units, a major advantage
8 of this approach is the ability to directly assess antibody labeling efficiency – a
9 necessity to unambiguously detect potential changes in nup composition at the
10 individual NPC level. For the central channel FG-nups and the scaffold elements of
11 the NPC including the cytoplasmic, nucleoplasmic and inner rings, we observed
12 specific and near-comprehensive labeling of the pan-stained NPCs (Figure 4d). In
13 contrast, the labeling of the nuclear basket nups NUP50, TPR and NUP153 and the
14 cytoplasmic filament nup Nup358 was notably less efficient (64-82%). Thus, it is
15 possible there are sub populations of NPCs that lack these asymmetric elements, in
16 line with observations in budding yeast that the presence of the nuclear basket
17 reflects an mRNA export state (Bensidoun et al., 2022).

18

19 **Pan-ExM reveals organization of NPCs in AL**

20 We next assessed whether Pan-ExM could be used to provide insight into the
21 composition and 3D organization of AL, which were robustly observed in an iPSC
22 line and were occasionally present in HeLa and SH-SY5Y cells. As expected from
23 prior EM studies (Cordes et al., 1996; Kessel, 1983), the NPCs in AL were organized
24 in densely stacked arrays that we present in both an en face (top-down; Figure 5a)
25 and lateral (Figure 5b) orientations. While EM favors efficient labeling of membranes,
26 we expected that the total protein labeling in Pan-ExM could provide new insight into
27 putative interactions between NPCs that may underlie the biogenesis of AL. Indeed,
28 the outer rings of the NPCs appeared to directly connect to NPCs both above and
29 below in two conformations (Figure 5c). In one, the NPCs were stacked on top of
30 each other such that the transport channels aligned. In another, the NPCs were
31 offset in a brick-like pattern. Most AL comprised a mixture of these two
32 arrangements. In principle, the observed juxtapositions of NPCs could be driven by
33 interactions between asymmetric elements of NPCs i.e. the cytoplasmic filaments
34 and nuclear basket, or between symmetric elements (i.e. the outer rings).

1
2 To test these models of NPC stacking in AL, we immunolabeled cells with nup
3 antibodies (Figure 5d). Whereas antibodies directed towards the FG-nups, NUP62
4 and NUP98, robustly labeled AL, we only observed sparse labeling of the
5 cytoplasmic filament nup NUP358 and, surprisingly, the transmembrane nups
6 POM121, NDC1 and GP210. We were unable to identify the basket component
7 NUP153 in AL stacks, despite clear NUP153 staining at NPCs embedded in the NE
8 in the same expanded cell. Thus, our observations, when taken together with other
9 studies including proteomic analyses of AL from *Drosophila* embryos (Hampoelz et
10 al., 2016; Hampoelz et al., 2019; Rasala et al., 2008; Walther et al., 2003), support
11 that NPCs in AL have reduced levels of transmembrane nups and lack the
12 asymmetric elements of the NPC. Thus, we favor the hypothesis that direct outer
13 ring interactions facilitate the NPC stacking underlying AL formation.

14

15 **POM121 localizes specifically to the nuclear ring**

16 Given our surprising observation that antibodies to transmembrane nups poorly label
17 AL (Figure 5d) despite efficiently labeling NPCs embedded in the NE (Figure 4d), we
18 were prompted to take a closer examination of their position in NPCs by Pan-ExM.
19 Indeed, although we understand the position of virtually all soluble nups within the
20 NPC, there remains uncertainty over the distribution of the pore membrane proteins,
21 particularly POM121. POM121 is not observed in cryo-EM maps despite strong *in*
22 *vitro* evidence suggesting that it is capable of biochemically interacting with
23 components of both the inner and outer rings (Yavuz et al., 2010), perhaps in a
24 mutually exclusive manner (Mitchell et al., 2010). Thus, in principle we would expect
25 that POM121 could localize to either the inner or outer rings (or both). We therefore
26 used Pan-ExM to test the distribution of POM121 by immunolabeling of expanded
27 HeLa cells. Interestingly, unlike antibodies directed to the other transmembrane
28 domain-containing nups, GP210 and NDC1, which stained the inner ring (Figure 4),
29 POM121 antibodies exclusively labeled the nuclear aspect of the NPC (Figure 6).
30 This surprising result was not unique to HeLa NPCs, as we observed the identical
31 asymmetry in the POM121 labeling of A549 and SH-SY5Y cells (Figure 6a, c).
32 Importantly, labeling of POM121 at this biased position was equally efficient as the
33 other pore membrane nups (compare Figure 6b and Figure 4d), suggesting the
34 robustness of this observation. Moreover, the favored position of POM121 labeling

1 (Figure 6c) most closely mimics the position of the nuclear ring staining of NUP107
2 (Figure 4c). Thus, POM121 is unique amongst the transmembrane nups and is
3 asymmetrically distributed in the NPC on the nuclear ring.

4 5 **POM121 shifts position in model ALS iPSNs**

6 To further push the boundaries of Pan-ExM and to investigate the potential functional
7 significance of POM121's specific localization to the nuclear ring, we tested whether
8 Pan-ExM could distinguish compositionally unique NPCs in the context of a
9 neurodegenerative disease model. Recent work supports that there is an NPC injury
10 cascade in which POM121 plays a critical role in the characteristic loss of a subset of
11 nups from NEs in iPSC derived neurons (iPSNs) from patients expressing a
12 hexanucleotide repeat expansion in *C9orf72*, the most common genetic cause of
13 ALS (Coyne et al., 2020). The observed NPC injury occurs approximately 32 days
14 after differentiation into motor neurons in culture. We therefore prepared
15 differentiated iPSNs at day 18 (before NPC injury) and day 32 (after NPC injury)
16 post-differentiation for examination by Pan-ExM. In all samples, NPCs were readily
17 visible in the pan-stain. Notably, while the extent of immunolabeling of NUP62
18 (previously found to be unaffected in this disease model (Coyne et al., 2021; Coyne
19 et al., 2020)) showed no change between day 18 and day 32 iPSNs (Supplementary
20 Figure 6), we observed a marked reduction in the labeling of POM121 (Figure 7a, b)
21 from 92% of NPCs at day 18 to 73% at day 32 specifically in *C9orf72* HRE-
22 expressing iPSNs but not the WT iPSN matched control. Prior studies have
23 suggested that loss of POM121 is a hallmark of a broader disruption in NPC
24 composition including diminished levels of seven other nups across multiple
25 subcomplexes (Coyne et al., 2020). Consistent with this, we also observed that
26 NPCs lacking POM121 have a statistically significant decrease in pan-labeling within
27 the segmented NPCs compared to POM121-containing NPCs in the same nucleus
28 (Figure 7c). Thus, Pan-ExM allows the visualization of pathological changes to the
29 biochemical identity of individual NPCs.

30
31 Most strikingly, upon close inspection of the anti-POM121 staining in the day 32
32 *C9orf72* HRE-expressing iPSNs, it was clear that in NPCs that retained POM121 it
33 was no longer distributed along the nuclear ring (Figure 7a, bottom right panel).
34 Indeed, in virtually all the antibody-labeled NPCs, the POM121 stain was now

1 mispositioned instead to the inner ring while the anti-POM121 labeling in WT iPSN
2 controls at the same timepoint retained the normal localization at the nuclear ring
3 (Figure 7a, d). Thus, using Pan-ExM we have visualized a remarkable response in
4 the position of a key transmembrane nup from the nuclear ring to the inner ring in a
5 pathological condition. While the underlying mechanism driving these changes
6 remains uncertain, we suggest that this may be an important, but to this point
7 invisible, step along the NPC injury cascade that may contribute to an ALS
8 pathomechanism.

9

10 **Discussion**

11 We have investigated the ability of Pan-ExM to serve as an enabling tool for
12 exploring several pressing questions in the nuclear transport field. We suggest that
13 Pan-ExM fills an important niche between cryo-EM/ET and super-resolution
14 microscopy. The Pan-ExM approach overcomes the significant financial, technical
15 and intellectual resources required for cryo-EM/ET while also circumventing the
16 modality-specific limitations of super-resolution imaging that are compounded by the
17 need to access specialized microscopes. Pan-ExM particularly excels at providing
18 insight into the molecular composition and structure (at tens of nanometer resolution)
19 at the level of individual NPCs in a given nucleus. As it is possible to perform Pan-
20 ExM on virtually any cell type and, with protocol modifications, tissues (M'Saad and
21 Bewersdorf, 2020; M'Saad et al., 2022), it promises to reveal a broad spectrum of
22 NPC diversity that has previously gone underappreciated. The ability to confidently
23 visualize NPCs of unique molecular composition and structure, as demonstrated
24 here, is the first step to understanding their function in both physiological and
25 pathological contexts.

26

27 As an example of a pathological context in which Pan-ExM was illuminating, we
28 investigated how NPCs change in an iPSN model of *C9orf72* ALS. The data first
29 reinforce that Pan-ExM can be used to assess the presence/absence of individual
30 nups from single NPCs, recapitulating the observed loss of POM121 during a
31 *C9orf72* HRE-specific NPC injury cascade thought to be central to an ALS
32 pathomechanism (Coyne and Rothstein, 2021; Coyne et al., 2020). While making a
33 definitive conclusion from negative data (i.e. lack of immunolabeling) is always
34 fraught, Pan-ExM has several key advantages over classic immunofluorescence and

1 super-resolution approaches that allows one to arrive at more confident conclusions.
2 First, the pan-stain recognizes virtually all NPCs. This provides a facile and
3 quantitative approach to establish the labeling efficiency per NPC for a given
4 antibody in a manner that is challenging or impossible for other methods. Labeling
5 efficiency is also greatly enhanced by expansion itself, overcoming epitope masking
6 that can occur in crowded macromolecular structures and facilitating efficient
7 penetration of antibodies into the sample (M'Saad and Bewersdorf, 2020). Indeed,
8 we observed that the tested antibodies recognizing scaffold nups label virtually all
9 NPCs (Figure 4d). Second, Pan-ExM revealed a remarkable change to the
10 nanoscale distribution of POM121 that occurred specifically in the *C9orf72* HRE-
11 expressing iPSN line 32 days after differentiation into motor neurons (Figure 7). The
12 timing is remarkable: precisely when NPC injury has been described to begin, we
13 observe that POM121 shifts position from the nuclear ring to the inner ring. We
14 suspect that this change precedes the complete loss of POM121 from NPCs (Figure
15 7b), at which time we observe a decrease in the total bulk protein at the NPC (Figure
16 7c). Thus Pan-ExM revealed a new step in the NPC injury pathway; moreover, this
17 finding suggests that there are changes in biochemical interactions among nups that
18 likely precedes their loss from the NPC. This work thus also reveals an aspect of
19 NPC plasticity that was previously unappreciated.

20

21 The underlying mechanism driving the shift in POM121 distribution remains
22 unknown, but as there is evidence that POM121 can biochemically engage with both
23 NUP160 and NUP155 in a mutually exclusive fashion (Mitchell et al., 2010), it is
24 attractive to consider the hypothesis that POM121 moves from a NUP160-bound
25 state (at the nuclear ring) to a NUP155-bound state (at the inner ring). While there
26 are many plausible mechanisms that may contribute to such a change including
27 putative post-translational modifications (Nino et al., 2016), another possibility is that
28 POM121's location reflects its engagement with nuclear transport receptors (NTRs).
29 POM121 is unique among the integral membrane nucleoporins in that it engages
30 directly with the Kap α /Kap β 1 NTR complex through a nuclear localization signal in
31 its N-terminus (Rasala et al., 2008; Yavuz et al., 2010). This NLS is thought to be a
32 key functional element that helps to target it to the inner nuclear membrane during
33 early steps of NPC biogenesis (Funakoshi et al., 2011; Talamas and Hetzer, 2011).
34 Interestingly, a previous study indicates that under conditions where POM121 binds

1 Kap α /Kap β 1 it displays strong binding to NUP155 but not NUP160 (Yavuz et al.,
2 2010). The release of Kap α binding occurs at the nuclear basket, predominantly
3 through a mechanism requiring NUP50; the NUP50 orthologue in budding yeast,
4 Nup2, is also essential for NLS-dependent targeting of integral membrane proteins to
5 the inner nuclear membrane (King et al., 2006; Lokareddy et al., 2015). Interestingly,
6 loss of NUP50 appears to be a critical component of NPC injury in ALS (Freibaum et
7 al., 2015; Megat et al., 2023). Thus, it is plausible that the unexpected and surprising
8 steady-state association of POM121 with the nuclear ring in model mammalian cell
9 lines is tied to disrupted release of Kap α and a preference for binding to NUP155.
10 This and the ultimate function of POM121 at the nuclear ring will be topics of future
11 work that will be supported by the unique ability of Pan-ExM to reveal positional
12 information of POM121 and other nups at the nanoscale.

13

14 While our discovery of biased positioning of POM121 at the nuclear ring of the NPC
15 was entirely unexpected, the ability of Pan-ExM to reveal a range of NPC diameters
16 across the same nucleus fills a critical need in the field. Indeed, approaches are
17 needed to interrogate the contexts and consequences of NE tension on NPC form
18 and function. Changes in NPC diameter have been proposed for decades, but only
19 recently with “in cellulo” cryo-ET of NPC structures has definitive evidence
20 supporting this type of NPC plasticity come to light (Akey et al., 2022; Mosalaganti et
21 al., 2022; Schuller et al., 2021; Zimmerli et al., 2021). Here, we provide a more
22 nuanced view of NPC diameter that supports that there is a spectrum of NPC dilatory
23 states with a bias for the most dilated NPCs to be on the basal nuclear surface. The
24 data further suggest that there are local islands (hundreds of square nanometers in
25 dimensions) of NPCs that are more or less dilated. As both the local islands and
26 basal bias of dilated NPCs are abolished upon ablation of LINC complexes, it is most
27 likely that NE tension, driven at least in part by cytoskeletal forces, can in fact
28 modulate NPC diameter. Such an idea may provide a function for the long-observed
29 association of SUN1 with NPCs (Liu et al., 2007; Talamas and Hetzer, 2011), and
30 may suggest a direct mechanoresponsive mechanism to dilate or constrict NPCs.
31 Although the idea that NE tension may impact NPC dilation has been proposed
32 (Elosegui-Artola et al., 2017; Mosalaganti et al., 2022; Schuller et al., 2021; Zimmerli
33 et al., 2021), this work reveals an additional nuance: that this tension may be much
34 more localized than previously thought. It remains mysterious, however, whether

1 these local NE tension differences can manifest actual functional changes to these
2 NPCs in their ability, for example, to establish a selective transport channel and/or
3 impact genome function, particularly as the relative mean changes in NPC diameter
4 at the NE in expanded samples appears modest. Interestingly, recent studies have
5 implicated SUN1 and LINC complex components as contributors to ALS
6 pathophysiology (Baskerville et al., 2024; Sirtori et al., 2024). Specifically, SUN1 may
7 be a critical mediator of passive permeability of the NPC (Baskerville et al., 2024).
8 Although the mechanisms underlying these events remain unknown, our work
9 suggests that Pan-ExM will likely be a useful tool for providing insight into these
10 neurodegenerative events.

11
12 Although one can easily measure NPC diameters in Pan-ExM samples, some
13 caution must be taken when using these measurements to calculate and compare
14 actual NPC diameters across samples as there are no perfect tools for precisely
15 calculating the experimental expansion factor, although the approach we take here
16 suggests that robust reproducibility is possible (Supplementary Figure 1).
17 Regardless, within a single sample one can quantitatively assess relative NPC
18 diameter changes. In this framework, the diameter differences that we observe from
19 evaluating the nuclear ring of the NPC are relatively modest, with NPCs on the
20 bottom versus the top of the nucleus differing by only <10%. However, the
21 quantitative effect on the inner ring is likely more pronounced given prior analysis of
22 how these different elements of the NPC respond to tension (Mosalaganti et al.,
23 2022; Schuller et al., 2021; Zimmerli et al., 2021). We do observe major changes in
24 NPC diameter by Pan-ExM at AL, where the diameters of the NPCs are ~35% more
25 constricted than those at the NE. Thus, we posit that the dimensions of the NPCs in
26 AL reflect a fully constricted state akin to what has been observed for NPC structures
27 in the context of perturbations like energy depletion, hyperosmotic shock, or
28 biochemical fractionation of NEs (Bui et al., 2013; von Appen et al., 2015; Zimmerli
29 et al., 2021). There are several implications of this hypothesis. First, it is likely that
30 LINC-complex dependent mechanotransduction mechanisms only modestly
31 modulate NPC diameter compared to the high variation across the NPC population
32 in an individual nucleus. Second, complete constriction of the NPC likely only occurs
33 under extreme environmental perturbation. In these scenarios, it may be logical for
34 cells to attempt to attenuate nuclear transport by “closing” their NPCs.

1
2 Another reason why NPCs may be fully constricted in AL is that they are in an
3 immature state. For example, NPCs in AL have also been suggested to lack key
4 components including the entirety of the nuclear basket (Hampoelz et al., 2016;
5 Hampoelz et al., 2019; Rasala et al., 2008; Walther et al., 2003). The underlying
6 mechanism for why AL NPCs are incompatible with nuclear basket assembly is not
7 understood. One possibility is that, as our data suggest, there are stacking
8 interactions between the outer rings of the NPCs in AL that preclude basket
9 assembly. An alternative model is that basket assembly may only occur in
10 membranes under tension. Such a concept aligns with work exploring the steps in de
11 novo NPC assembly where the basket is curiously added as a terminal step
12 (Onischenko et al., 2020; Otsuka et al., 2023). Further, during post-mitotic NPC
13 assembly early intermediates are assembled into a small nuclear pore before it
14 dilates to complete assembly (Otsuka et al., 2018). More broadly, this interpretation
15 invites the idea that NE tension could directly impact NPC composition. For example,
16 during zebrafish embryonic development NPCs are thought to mature from a
17 constricted state lacking the nuclear basket to a more mature, transport-competent
18 form after the maternal to zygotic transition (Shen et al., 2022). It also has
19 implications for mechanotransduction mechanisms – for example, the local
20 modulation of tension could favor/disfavor the stable incorporation of nuclear basket
21 proteins, which could direct RNA export, for example, to biochemically polarized
22 NPCs. Our hope is that Pan-ExM will provide a key tool to begin to test these and
23 other hypotheses.

24

25

26

1 **METHODS**

2 **Cell culture**

3 HeLa cells were cultured in Dulbecco's modified Eagle medium (DMEM; Gibco,
4 11965092) supplemented with 10% fetal bovine serum (FBS; Gibco, A5256801),
5 penicillin-streptomycin mix (pen/strep; Gibco, 15140122) and sodium pyruvate
6 (Gibco, 11360070). A549 cells were cultured in DMEM F12 (Gibco, 11320032) with
7 10% FBS and pen/strep. SH-SY5Y cells were cultured in Eagle's Minimum Essential
8 Medium (EMEM; ATCC, 30-2003) with 15% heat inactivated FBS, pen/strep and 2
9 mM Glutamax (Gibco, 35050061). iPSCs were grown on Geltrex (Thermo Scientific,
10 A1413302) coated plates and cultured in mTESR1 media (Stem Cell Technologies,
11 85850). All cells were maintained at 37°C with 5% CO₂. Passaging was performed
12 using 1X PBS and 0.05% Trypsin (Gibco, 25300054) or 0.5 mM EDTA (Corning, 46-
13 034-CI) for iPSCs. 24 h before fixation, ~65,000 cells were seeded onto coverslips
14 coated with 50 µg/mL collagen (Corning, 354236).

15

16 **Direct-induced motor neuron differentiation**

17 *C9orf72* ALS patient and control iPSCs (Supplementary Table 1) were obtained from
18 the Answer ALS repository at Cedars Sinai and differentiated into spinal motor
19 neurons as previously described following a modified direct-induced motor neuron
20 differentiation protocol (Baskerville et al., 2024; Coyne et al., 2020). iPSNs were
21 cryopreserved in Cryostor CS10 media on day 12 of differentiation. Briefly, iPSNs at
22 day 12 of differentiation were thawed and grown on Matrigel (Corning, CLS35623)
23 coated dishes and cultured in stage 3 media composed of 47.5% Iscove's modified
24 Dulbecco's medium (IMDM; Gibco, 12440061), 47.5% F12 (Gibco, 11765054) with
25 2% B-27 (Gibco, 17504044), 1% MEM Non-Essential Amino Acids (NEAA; Gibco,
26 11140050), 1% N-2 (Gibco, 17502048), pen/strep, 2.5 µM DAPT (Sigma-Aldrich,
27 D5942), 0.5 µM all-trans retinoic acid (RA; Sigma-Aldrich, R2625), 0.1 µM
28 Compound E (Sigma-Aldrich, 565790), 0.1 µM dibutyryl-cAMP (Santa Cruz
29 Biotechnology, sc-201567), 0.1 µM SAG (Cayman Chemical Company, 11914), 200
30 ng/mL Ascorbic acid (Sigma-Aldrich, A4544), 10 ng/mL BDNF (PeproTech, 450-02)
31 and 10 ng/mL GDNF (PeproTech, 450-10). Media was exchanged every 3 days.

32

33

34

1 **CRISPR guide plasmid cloning**

2 Guides targeting *Sun1* and *Sun2* were cloned into the pSpCas9(BB)-2A-Puro
3 (PX459) plasmid (Addgene, 48139) as follows. Primers containing the guide
4 sequences flanked by BbsI (Bpil) cut sites were generated for each gene of interest.
5 Guide sequences for *Sun1* and *Sun2* (Supplementary Table 2) were selected from
6 the Toronto Knockout Library V3(Hart et al., 2017). An additional G nucleotide was
7 added between the BbsI sequence and the guide sequence if the guide sequence
8 did not begin with a G or C. Primers were phosphorylated using a T4 polynucleotide
9 kinase reaction incubated at 37°C for 30 minutes and annealed by bringing the
10 temperature of the reaction from 95°C to 25°C, decreasing by 10°C every minute.
11 The pX459 plasmid was digested using BbsI. The plasmid and guides were
12 annealed using Quick Ligase and transformed into DH5alpha cells. Plasmids were
13 isolated and sequenced to confirm correct guide integration.

14

15 ***Sun1*^{-/-}/*Sun2*^{-/-} double knock-out A549 cell line generation**

16 All eight guide plasmids (4 for *Sun1* and 4 for *Sun2*) were transfected into A549 cells
17 using the Amaxa Cell Line Nucleofector Kit T (Lonza Bioscience, VCA-1002)
18 according to the manufacturer's instructions and plated into a 10cm plate in
19 A549 media. 48 hours post-transfection, cells were selected using 0.5 µg/mL
20 puromycin in A549 media for 1 week, changing the media every 3 days. After
21 selection, cells were plated at a limiting dilution (0.5 cells / well) into 96-well plates
22 and assessed for colony formation over the following 7-14 days. Wells with single
23 colonies were subsequently expanded and tested for knock-out using a combination
24 of immunofluorescence staining, western blotting, and sequencing (see
25 Supplementary Figure 4).

26

27 **Cell line validation via gDNA sequencing**

28 Genomic DNA was harvested from clonal cell lines using QuickExtract (Lucigen,
29 QE09050) according to the manufacturer's instructions. Primers were designed to
30 amplify 400 – 600 bp regions containing the guide target site (Supplementary Table
31 3). Regions of interest were amplified using iProof High-Fidelity DNA polymerase
32 (Bio-rad, 1725301) and sequenced. Sequences were analyzed for the presence of
33 InDels using Synthego ICE analysis (<https://ice.synthego.com>).

34

1 **Pan-ExM**

2 Pan-ExM was performed as previously described (M'Saad and Bewersdorf, 2020).
3 Cells were fixed in 4% formaldehyde (FA; Electron Microscopy Sciences, 15710) in
4 1X PBS for 1 h at RT. Samples were rinsed with 1X PBS three times and post-fixed
5 in 0.7% FA and 1% acrylamide (AAm; Sigma, 01697) in 1X PBS for 6 h at 37°C.
6 Next, samples were washed three times with 1X PBS for 15 min each on a rocking
7 platform and embedded in the first gelling solution (19% sodium acrylate (SA;), 10%
8 AAm, 0.1% N,N'-(1,2-dihydroxyethylene)bisacrylamide (DHEBA; Sigma, 294381),
9 0.25% Ammonium persulfate (APS; BioRad, 1610700) and 0.25%
10 tetramethylethylenediamine (TEMED; Sigma, T7024) in 1X PBS within custom-
11 constructed gelation chambers for 1.5 h at 37°C in a humidified container. Samples
12 were then incubated in denaturation buffer (200 mM sodium dodecyl sulfate (SDS;
13 Sigma, 75746) , 50 mM tris [hydroxymethyl] aminomethane (Tris; Sigma, T6066), 50
14 mM sodium chloride (NaCl; JT Baker, 3627-07), pH 6.8 for 15 min at 37°C. Gels
15 were then transferred to 1.5 mL Eppendorf tubes containing denaturation buffer and
16 incubated for 1h at 73°C, then washed three times with 1X PBS for 20 min each on a
17 rocking platform at RT.

18
19 For the first expansion, gels were placed in MilliQ water twice for 30 min each then
20 for 1 h. Expanded gels were then incubated in a second gelling solution (10% AAm,
21 0.05% DHEBA, 0.05% APS and 0.05% TEMED) twice for 20 min each on a rocking
22 platform at RT. After removal of residual solution, gels were sandwiched between a
23 microscope slide and No. 1.5 coverslip, placed in a humidified degassing chamber
24 and perfused with nitrogen gas for 10 min. The chamber was then sealed and
25 incubated for 1.5 h at 37°C.

26
27 Next, gels were incubated in a third gelling solution (19% SA, 10% AAm, 0.1% N,N'-
28 methylenebis(acrylamide) (BIS; Sigma, 14602), 0.05% APS and 0.05% TEMED)
29 twice for 15 min each on a rocking platform on ice. After removal of residual solution,
30 gels were sandwiched between a microscope slide and No. 1.5 coverslip, placed in a
31 humidified degassing chamber and perfused with nitrogen gas for 10 min. The
32 chamber was then sealed and incubated for 1.5 h at 37°C. To dissolve DHEBA
33 crosslinks, gels were incubated in 200 mM NaOH (Macron, 7708-10) for 1 h on a

1 rocking platform at RT. Gels were then washed three times with 1X PBS for 20 min
2 each on a rocking platform at RT.

3

4 **Immunostaining of Pan-ExM samples**

5 For immunostaining, gels were incubated in primary antibodies (Supplementary
6 Table 4) diluted to 1:500 in antibody dilution buffer (2% bovine serum albumin (BSA;
7 Sigma, A9647) in 1X PBS) for 24 h. Gels were washed three times with PBS-0.1%
8 Tween (PBS-T) for 20 min each, then for 12 h. Next, gels were incubated in
9 secondary antibodies diluted to 1:500 in antibody dilution buffer for 12 h. Gels were
10 washed three times with PBS-T for 20 min each, then for 12 h. All steps were
11 performed on a rocking platform at RT.

12

13 **Pan-staining and SYTOX Green staining**

14 Gels were incubated in 20 µg/mL NHS ester CF568 (Biotium, 92131) in 100 mM
15 sodium bicarbonate solution (JT Baker, 3506-01) for 1.5 h on a rocking platform at
16 RT. Gels were then washed three times with PBS-T for 20 min each. Next, gels were
17 incubated in SYTOX Green (Thermo Scientific, S7020) diluted to 1:3,000 in calcium
18 and magnesium free HBSS buffer (Gibco, 14170112) for 1 h on a rocking platform at
19 RT. Gels were then washed three times with PBS-T for 20 min each.

20

21 **Pan-ExM second expansion and sample mounting**

22 Antibody labeled and stained gels were placed in MilliQ water twice for 30 min each
23 then for 1 h. Expanded gels were mounted on 30 mm No. 1.5 glass bottom MatTek
24 dishes with an 18 mm round coverslip on top, and sealed with a two-component
25 silicone (Picodent, 13001000). Samples were then stored in the dark at RT until
26 imaging.

27

28 **Image acquisition**

29 Data acquisition was carried out on a Dragonfly confocal microscope (Andor) with a
30 water immersion 60x 1.2 NA objective. Fusion software (Andor) was used to control
31 imaging parameters. SYTOX Green, CF568 Succinimidyl ester and ATTO647N were
32 imaged with 488-nm, 561-nm and 647-nm excitation, respectively. Entire cell
33 volumes were acquired by performing z-stack tile scans using a 0.25 µm step size.

34

1 **Image analysis and visualization**

2 3D reconstruction, volume rendering, and analysis of Pan-ExM images was
3 performed using Imaris versions 9.9-10.2 (Andor). Images and movies were
4 generated using the snapshot and animation tools. Cellular structures were
5 segmented as Imaris Surface, Spot or Cell objects depending on the parameters to
6 be calculated and the object-object statistics to be measured.

7

8 **Nuclei segmentation**

9 Nuclei were segmented as surface objects by LABKIT machine learning pixel
10 classification of all acquired channels (SYTOX, NHS ester Pan-stain and antibody
11 channels) by manual annotation of foreground and background pixels. A binary mask
12 nucleus channel was then created to account for SYTOX bleaching over large
13 cellular volumes and in stitched images. The masked nucleus channel was used to
14 generate a cell object to measure nuclear volume, surface area, object-orientated
15 bounding box lengths and sphericity.

16

17 **Total NPC segmentation**

18 To segment all NPCs, regions of interest (ROIs) of a subset of images containing
19 pan-stain and masked nucleus channels were manually annotated in LABKIT. NPC
20 nuclear ring structures were labeled as foreground pixels and iterative training
21 performed until the classifier was able to consistently recognize NPCs in all axial
22 orientations. Performance was assessed by manual inspection of segmentation
23 results and comparing the number of segmented NPCs and number of segmented
24 nup antibody surfaces identified at the NE. To enable quantification of average
25 distances to nearest neighbor objects, a binary mask total NPC channel was created
26 and spot objects with an estimated XY diameter of 0.75 μm (value not corrected for
27 expansion) automatically generated.

28

29 **NPC diameter segmentation**

30 Given that the total NPC classifier was optimized for robust identification of NPCs
31 across different cells, a separate classifier was trained in LABKIT to accurately
32 measure nuclear ring NPC diameter. ROIs of images containing pan-stain and
33 SYTOX channels were manually annotated, with NPC nuclear ring structures labeled
34 as foreground pixels. Iterative training was conducted until the classifier consistently

1 segmented the oblate spheroids surfaces corresponding to regions at the NE that
2 were intensely pan-stained and devoid of SYTOX. NPC diameter was quantified as
3 the average of the lengths B and C of the object-orientated bounding box
4 surrounding the segmented nuclear ring NPC surfaces. NPC position at the top or
5 bottom of the nucleus was determined by z-position values.

6

7 NPC diameter surface objects were then filtered and split into quintiles based on
8 size. A random 20% of NPC diameter surface objects class was also generated by
9 manual selection of object IDs via a random number generator in Excel. Binary mask
10 NPC diameter channels were created and spot objects with an estimated XY
11 diameter of 0.75 μm (value not corrected for expansion) automatically generated for
12 each NPC diameter class to enable quantification of average distance to nearest
13 neighbor objects. To visualize NPC clustering by size, NPCs were color-coded by
14 NPC diameter class and overlaid on 3D renderings of the nuclear surface. NPC
15 diameter was measured at AL by training a classifier to segment NPC rings visible in
16 top-down view AL stacks on the basis of the pan-stain channel only.

17

18 **Nup antibody segmentation**

19 Nup antibody signal was automatically segmented in Imaris as surface objects using
20 a background subtraction algorithm and the same manually determined threshold
21 and smoothing settings for each antibody within a set of experiments. Segmented
22 nup antibody surface objects of less than 5 voxels were filtered out. Nup antibody
23 signal was also automatically segmented as spot objects with an estimated XY
24 diameter of 0.75 μm (value not corrected for expansion) and background subtraction
25 selected. Segmentation was performed on entire images to enable identification of
26 antibody distributed at the NE and at AL.

27

28 **AL segmentation**

29 To segment AL, ROIs of pan-stain channel images were manually annotated in
30 LABKIT and surface objects created by iterative training.

31

32 **Nup antibody labeling of NPCs analysis**

33 To quantify nup antibody labeling efficiency, the shortest distance from the border of
34 each segmented NPC surfaces to the border of segmented nup antibody surfaces

1 was computed automatically in Imaris. NPCs were classified as labeled if antibody
2 signal was within 2 μm (value not corrected for expansion).

3

4 **Nup antibody position analysis**

5 To determine the precise location of nup antibody labeling at NPCs, the shortest
6 distance from the border of the segmented nuclear surface to the center of
7 segmented nup antibody spots was computed automatically in Imaris. Values were
8 normalized to the position of NUP107 to define the 'middle' of NPCs.

9

10 **Expansion factor measurement**

11 Expansion factors were determined for each experiment by averaging peak-to-peak
12 distances of line profiles drawn through centrioles and mitochondria in expanded
13 samples using the Spots Intensity Profile Imaris XTension in MATLAB (Mathworks).
14 These values were divided by the previously determined dimensions of structures
15 measured by EM to estimate the linear expansion factor.

16

17 **Statistical analysis**

18 Statistical analyses were performed using Prism 9.4.1 software (GraphPad).
19 Unpaired t-tests, ordinary one-way ANOVA with Tukey's multiple comparisons test or
20 Kruskal-Wallis test with Dunn's multiple comparisons test were used, as denoted in
21 the figure legends, to assess significance, defined as $p < 0.05$.

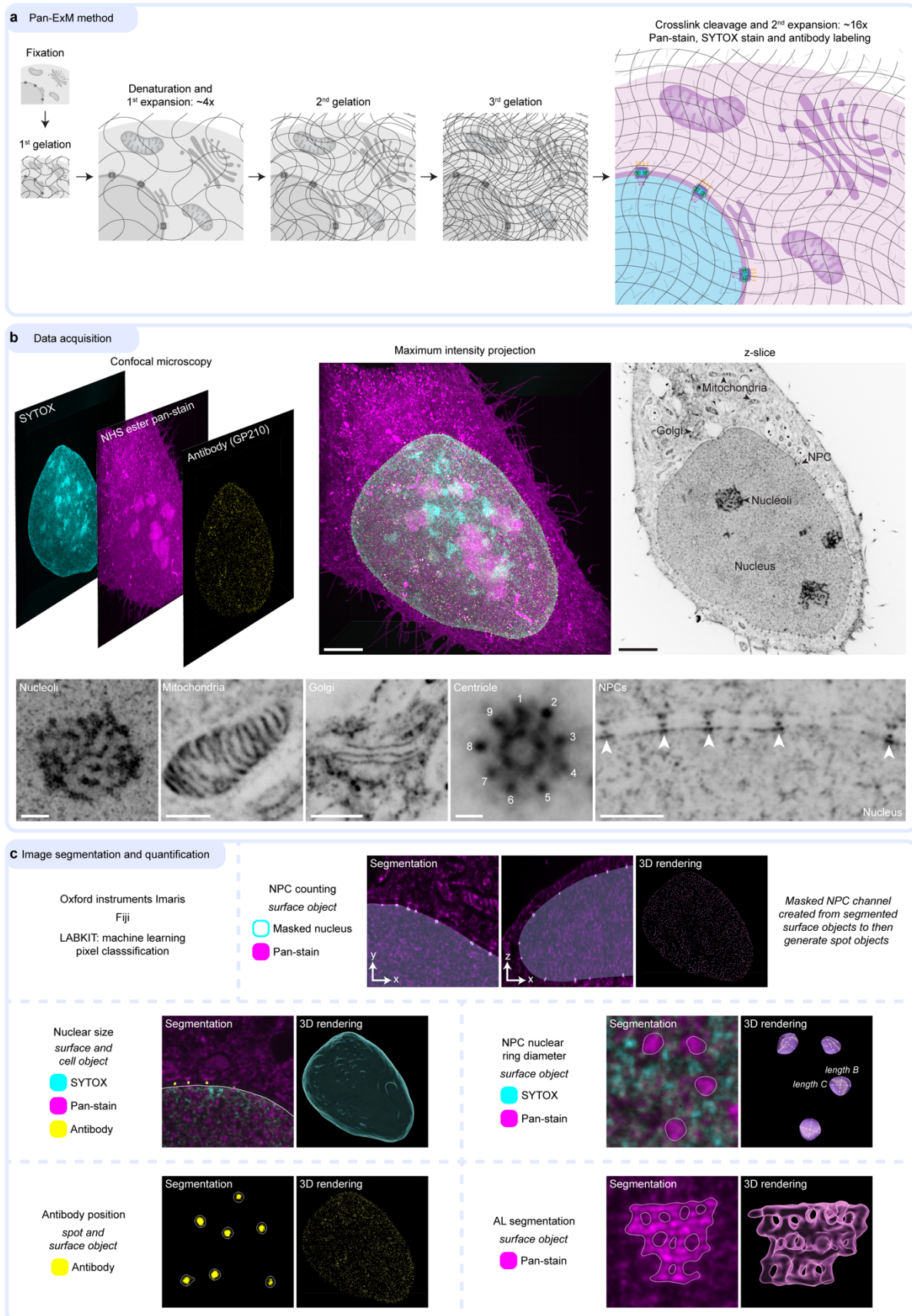
22

23 **Acknowledgments**

24 We thank Sunandini Chandra for assistance with iPSN cell cultures, Elisa Rodriguez
25 for her invaluable support, and all members of the LusKing laboratory for discussion
26 and feedback. We thank Yuan Tian, Phylcia Kidd and the entire Bewersdorf lab for
27 assistance with Pan-ExM. We thank the ALS patients and their families for essential
28 contributions to this research. This work was funded by the National Institutes of
29 Health R01 NS122236 (to CPL and JDR), F31 HL158119 (to EC), and R01
30 GM129308 (to MCK).

31

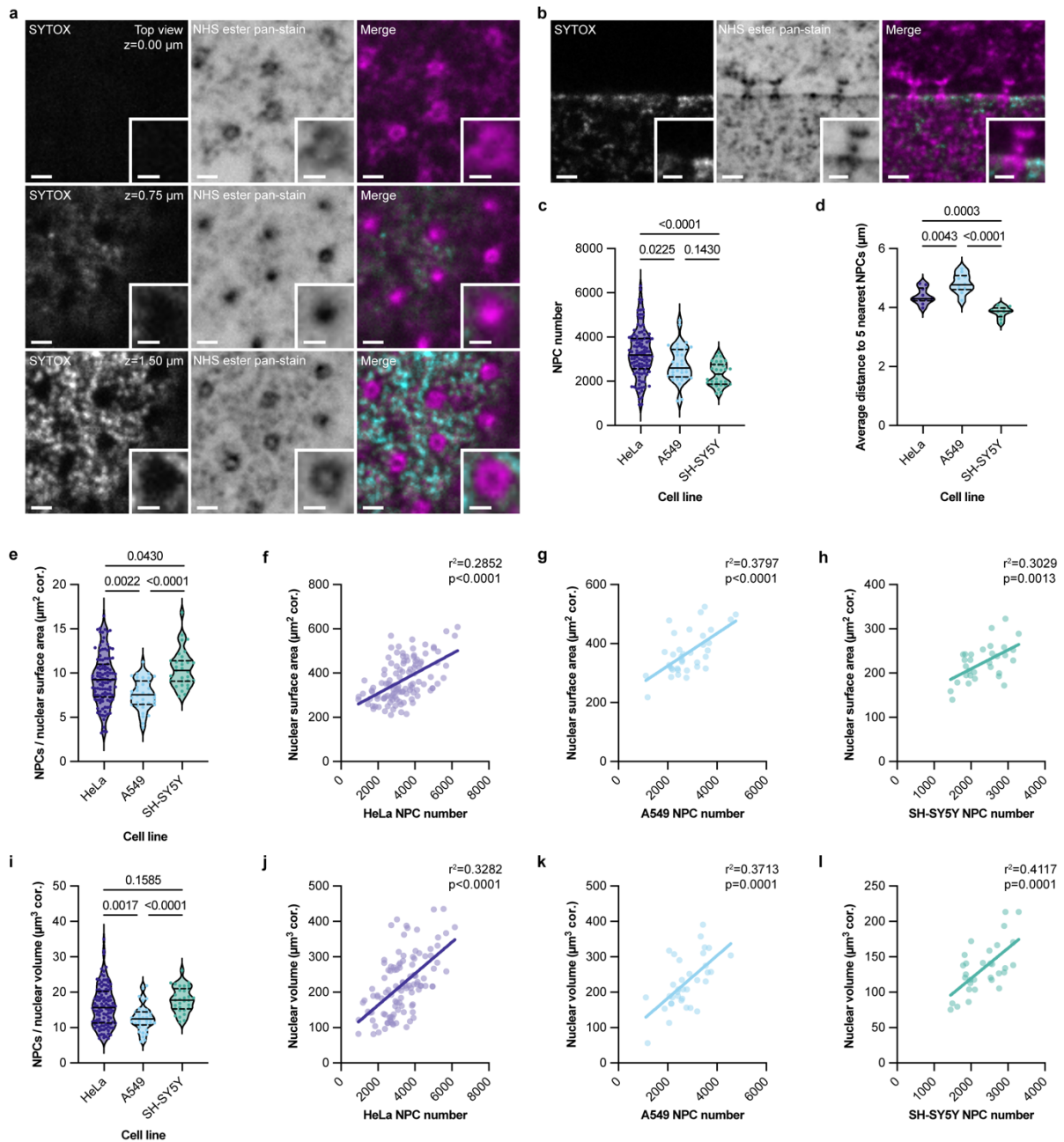
32



1

2 **Figure 1. Workflow and image analysis pipeline to visualize and analyze NPCs**
3 **using Pan-ExM**

1 **a.** Schematic of the Pan-ExM method adapted from M'Saad and Bewersdorf, 2020.
2 **b.** Overview of Pan-ExM data acquisition by confocal fluorescence microscopy with
3 representative single-channel images of an expanded HeLa cell stained with SYTOX
4 green, NHS ester pan-stain and labeled with an antibody against the nucleoporin
5 GP210. Whole cell volumes can be imaged and visualized as desired - a maximum
6 intensity projection merge and single channel z-slice (inverted) shown as examples.
7 Scale bars 30 μm . The ultrastructure of nucleoli, mitochondria, Golgi stacks,
8 centrioles and NPCs (arrows) are revealed by the pan-stain, shown with an inverted
9 color table. Scale bar 1 μm for centriole panel and 5 μm for all other panels. **c.**
10 Development of image analysis pipelines using Imaris software with the Fiji plugin
11 LABKIT to segment and visualize cellular structures in 3D. Utilizing the denoted
12 image channels and object creation modules (surface, spot and cell) in Imaris;
13 NPCs, nuclei, antibody signal and annulate lamellae (AL) were segmented.
14 Representative images of segmentation results are outlined in single z-slices and 3D
15 renderings are shown.
16
17

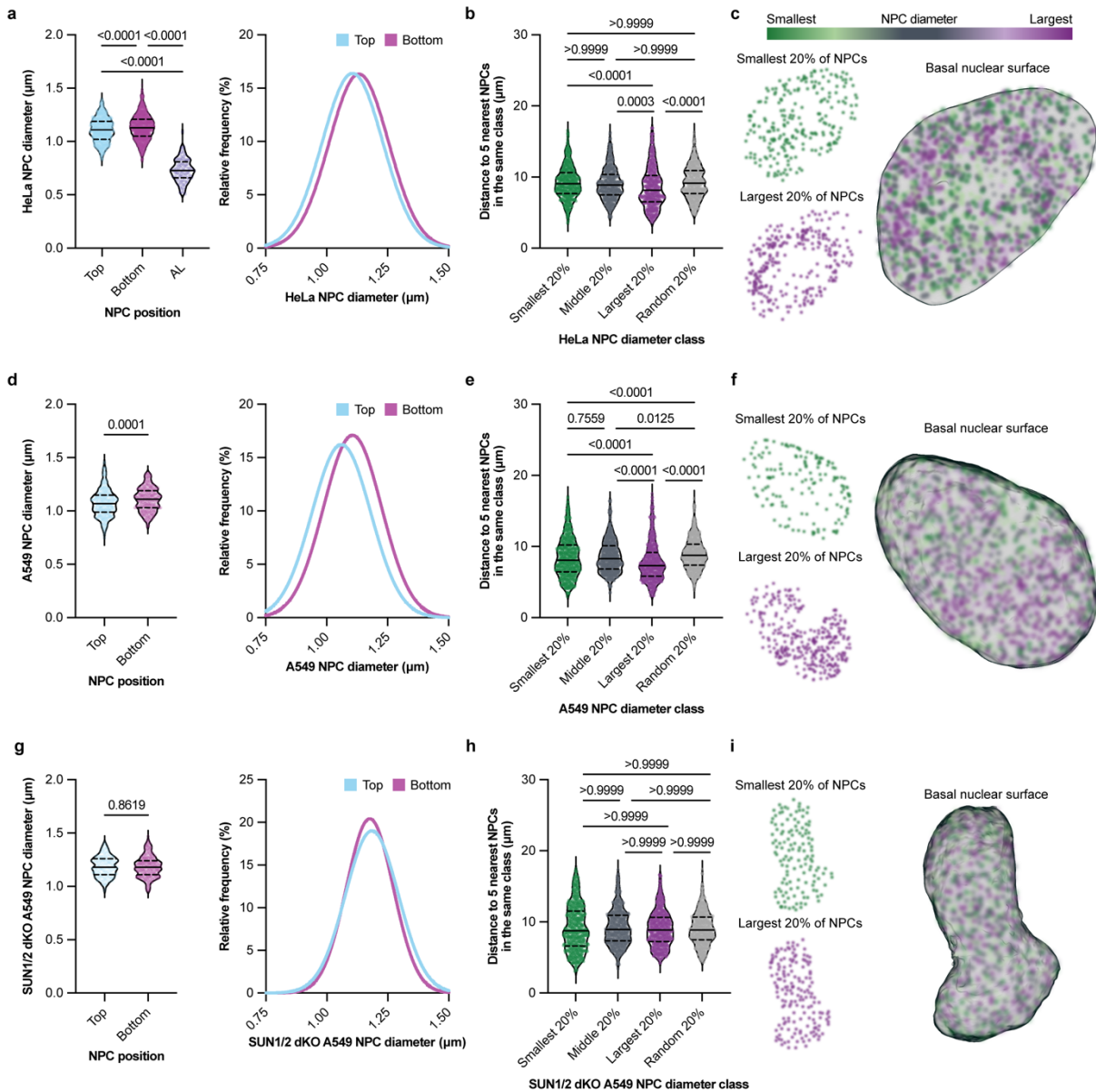


1
 2
 3
 4
 5
 6
 7
 8
 9
 10
 11

Figure 2. Comprehensive visualization of NPCs with Pan-ExM reveals characteristic NPC density and distribution across representative cell lines

a-b. Representative confocal fluorescence microscopy images of NPCs in expanded HeLa cells stained with SYTOX and NHS ester pan-stain at indicated axial positions (a) and in cross-section (b). Scale bars 2 μm. Insets show magnified view of the NPC, scale bars 1 μm. **c.** Total NPC number is variable and highest in expanded HeLa cells compared to A549 and SH-SY5Y cells. n=31 SH-SY5Y cells from 2 independently expanded samples, n=36 A549 cells from 2 independently expanded samples, n=114 HeLa cells from 4 independently expanded samples. Median values shown as solid lines and quartile values shown as dashed lines. Ordinary one-way

1 ANOVA with Tukey's multiple comparisons test. **d.** NPCs are most clustered in SH-
2 SY5Y cells. Average distance to the five nearest NPCs measured in cells
3 representative of local NPC density in each cell line. n=10 cells per line. Median
4 values shown as solid lines and quartile values shown as dashed lines. Ordinary
5 one-way ANOVA with Tukey's multiple comparisons test **e.** Overall NPC density
6 (NPCs per nuclear surface area corrected "cor." for the determined expansion factor)
7 is variable across the population but highest in SH-SY5Y cells. Median values shown
8 as solid lines and quartile values shown as dashed lines. Ordinary one-way ANOVA
9 with Tukey's multiple comparisons test. **f-h.** Total NPC number trends with nuclear
10 surface area but with substantial variability. Lines represent a simple linear
11 regression with the coefficient of determination (r^2) indicated. **i.** Total NPC number
12 per nuclear volume (corrected for the determined expansion factor) is more
13 characteristic than NPC density on the nuclear surface. Median values shown as
14 solid lines and quartile values shown as dashed lines. Ordinary one-way ANOVA
15 with Tukey's multiple comparisons test. **j-k.** NPC number generally correlates better
16 with nuclear volume than nuclear surface area (compare to f-h). Lines represent a
17 simple linear regression with the coefficient of determination (r^2) indicated.
18
19

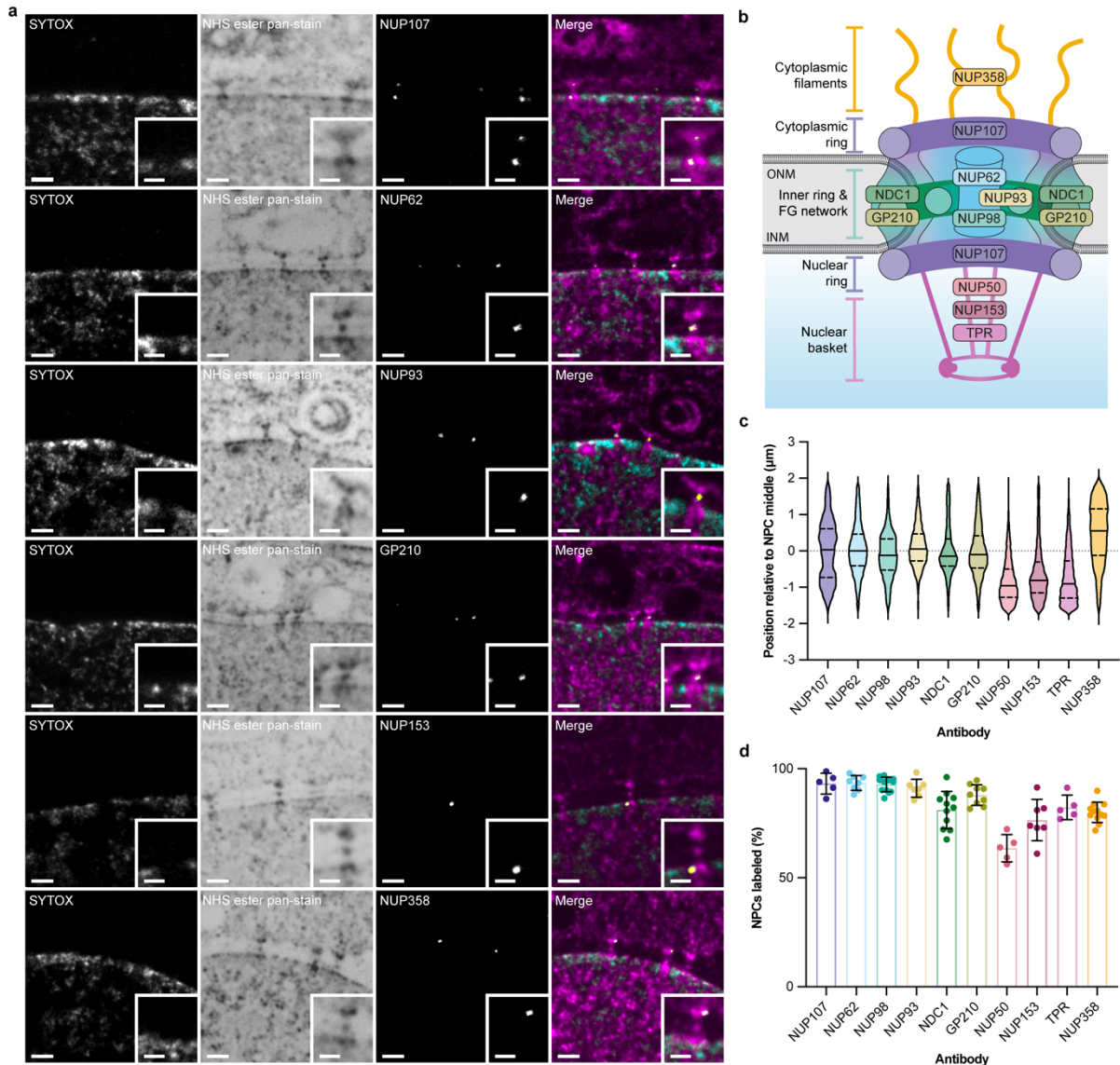


1

2 **Figure 3. Pan-ExM reveals LINC complex-dependent, local differences in NPC**
 3 **diameter**

4 **a.** The nuclear ring of NPCs at the bottom (closest to the basal cell surface) of the
 5 nucleus are dilated compared to those at the top, but all NE-embedded NPCs are
 6 dilated compared to those in AL. Diameter measured at the top and the bottom of the
 7 nucleus, and in AL, in HeLa cells. Results also shown as relative frequency
 8 distributions with Gaussian curve fitting. $n=2335$ NPCs in $n=10$ HeLa cells from a
 9 single expansion. **b.** NPCs are more likely to reside near neighboring NPCs of like
 10 diameter. Average distance to the five nearest NPCs within the same diameter class
 11 in a single HeLa nucleus. $n=1984$ NPCs. **c.** Visualization of NPC distribution
 12 according to dilation state at the basal nuclear surface of a HeLa cell by color-coding

1 according to NPC diameter class. The most constricted 20% of NPCs are shown in
2 dark green, and the most dilated 20% are shown in dark purple. All NPCs are
3 overlaid on a 3D rendering of the nucleus. **d, e, f.** The same trends in greater NPC
4 dilation on the bottom of the nucleus (n=709 NPCs in n=4 cells from a single
5 expansion) and clustering of NPCs (n=2412) of like diameter is also observed in
6 A549 cells. **g.** Disrupting LINC complexes by CRISPR ablation of *Sun1* and *Sun2*
7 (SUN1/2 dKO) leads to a loss of the bias for greater NPC dilation on the bottom of
8 the nucleus (n=521 NPCs in n=3 SUN1/2 dKO A549 cells from a single expansion).
9 **h, i.** Disrupting LINC complexes leads to homogenization of NPC diameter across
10 the nuclear surface (n=2296 NPCs). For all plots, median values shown as solid
11 lines and quartile values shown as dashed lines. Statistical analysis by ordinary one-
12 way ANOVA with Tukey's multiple comparisons test (a), the Kruskal-Wallis test with
13 Dunn's multiple comparisons test (b, e, h) or unpaired t-test (d, g).
14



1

2 **Figure 4. Nup antibody labeling establishes the ability of Pan-ExM to reveal**
 3 **nup position within the NPC ultrastructure**

4 **a.** Representative confocal fluorescence microscopy images of NPCs in expanded
 5 HeLa cells stained with SYTOX, NHS ester pan-stain, and labeled with antibodies
 6 against the indicated nups affirms their localization to the expected NPC subunit.

7 Scale bars 2 μm . Insets show a magnified view of the NPC, scale bars 1 μm . **b.**

8 Schematic of the NPC with established nup positions and NPC architectural subunits

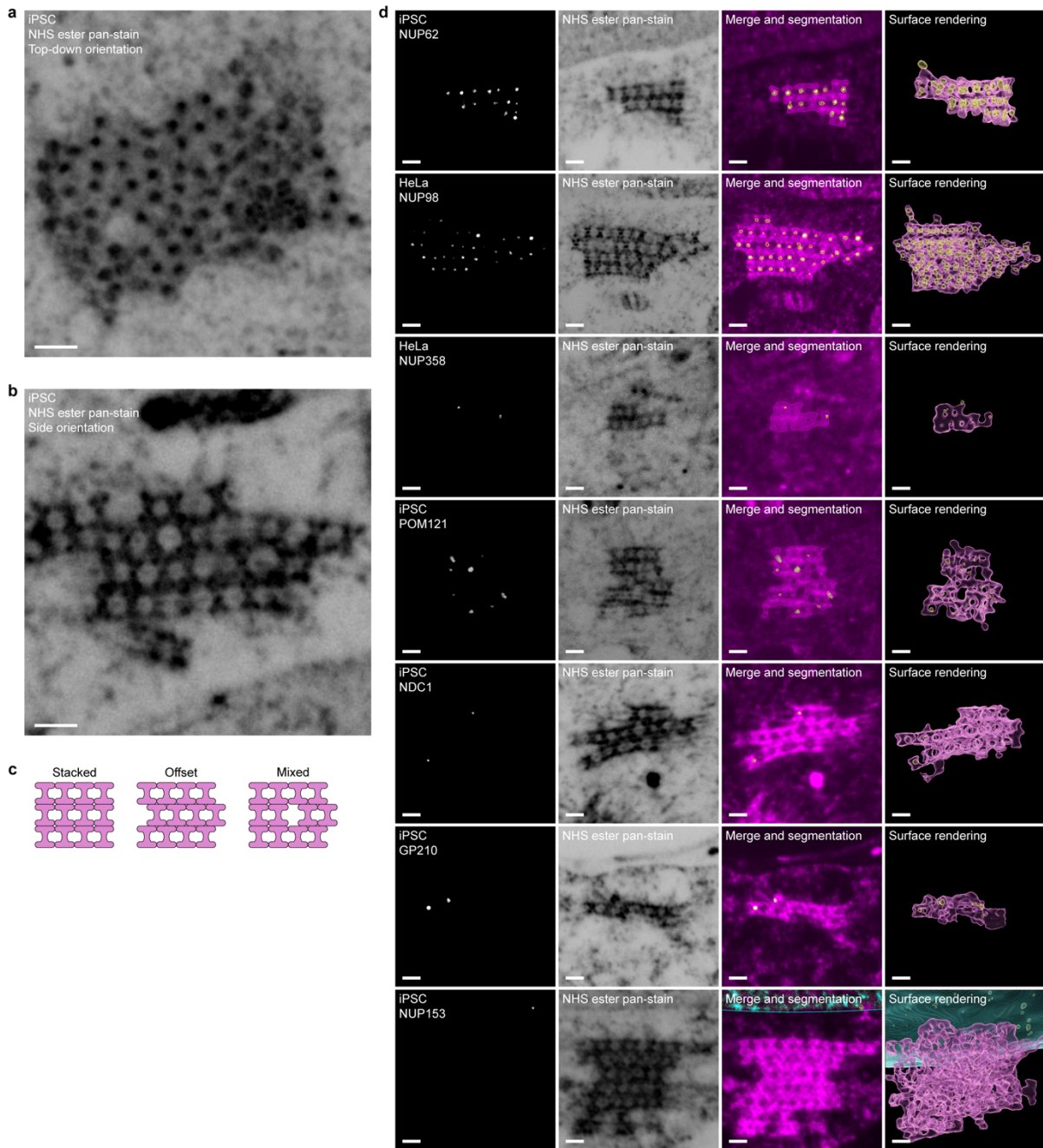
9 indicated. ONM: outer nuclear membrane, INM: inner nuclear membrane. **c.** Spatial
 10 distribution of nup antibodies along the transport axis in HeLa cells relative to the

11 NPC middle denoted by the dotted line reinforces the ability of PanExM to faithfully

12 retain established NPC architecture. Median values shown as solid lines and quartile

13 values shown as dashed lines. n=2451 segmented NUP107 spots in n=2 cells,

1 n=9676 segmented NUP62 spots in n=4 cells, n=4083 segmented NUP98 spots in
2 n=2 cells, n=1242 segmented NUP93 spots in n=1 cell, n=13831 segmented NDC1
3 spots in n=7 cells, n=12213 segmented GP210 spots in n=6 cells, n=2079
4 segmented NUP50 spots in n=5 cells, n=3988 segmented NUP153 spots in n=4
5 cells, n=7603 segmented TPR spots in n=5 cells, n=855 segmented NUP358 spots
6 in n=1 cell. Cells from 1-2 independently expanded samples. **d.** Nearly all NPCs
7 segmented based on the NHS ester-pan stain were labeled with antibodies to the
8 inner ring and nuclear/cytoplasmic ring components whereas the peripheral nups
9 were detected at most but not all NPCs. Percentage of NPCs per nuclei labeled with
10 nup antibody in HeLa cells. Bars and error bars are the mean and s.d., respectively.
11 n=82 cells from 4 independently expanded samples.
12



1
2 **Figure 5. Pan-ExM reveals organization of annulate lamellae**
3 **a-b.** Stacks of AL – NPCs embedded in the endoplasmic reticulum – can be readily
4 identified by their ultrastructure in Pan-ExM samples. Representative confocal
5 fluorescence microscopy images of AL of expanded iPSCs stained with NHS ester
6 pan-stain in top-down (a) and side view (b) orientations. Scale bars 2 μ m. **c.** The
7 organization of individual NPCs in AL ranges from stacked, to offset, or a mixture as
8 illustrated in the schematics. **d.** NPCs in AL are readily stained with antibodies to the
9 FG-nups but are sparsely labeled with antibodies to the transmembrane nups or
10 asymmetric NPC elements. Representative confocal fluorescence microscopy

1 images of AL in expanded iPSC and HeLa cells labeled with antibodies against the
2 indicated nups, and stained with NHS ester pan-stain. 3D surface renderings of
3 segmented structures are also shown. Scale bars 2 μ m.

4

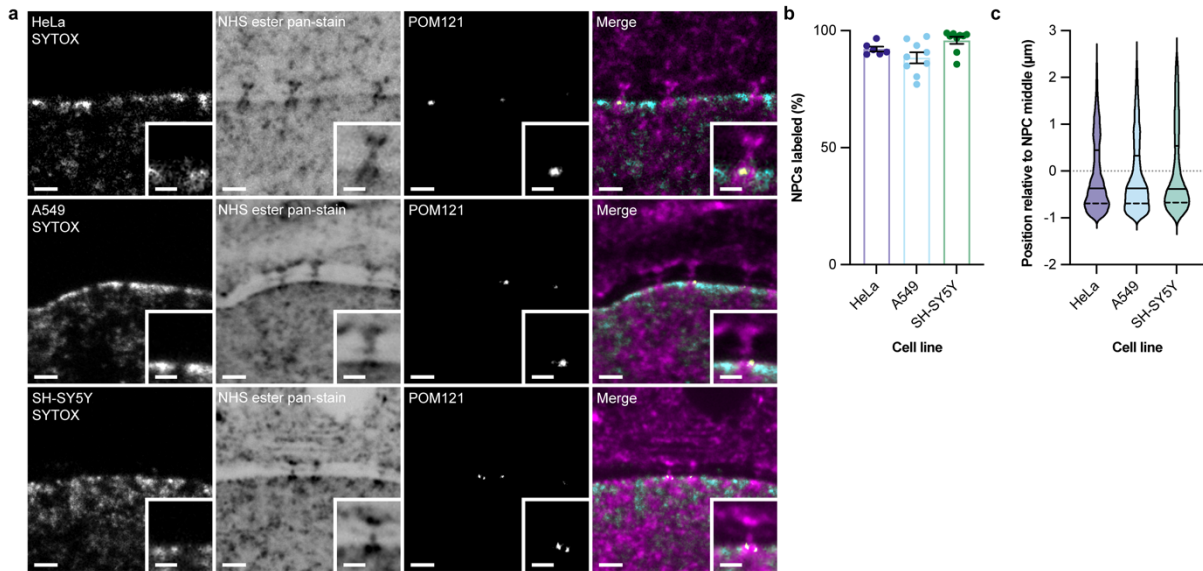


Figure 6. POM121 localizes specifically to the nuclear ring of NPCs

a. POM121 shows a biased distribution towards the nuclear ring of the NPC.

Representative confocal fluorescence microscopy images of NPCs in expanded cells of the indicated cell line stained with SYTOX, NHS ester pan-stain, and labeled with an antibody against POM121. Scale bars 2 μm. Insets show a magnified view of the NPC, scale bars 1 μm.

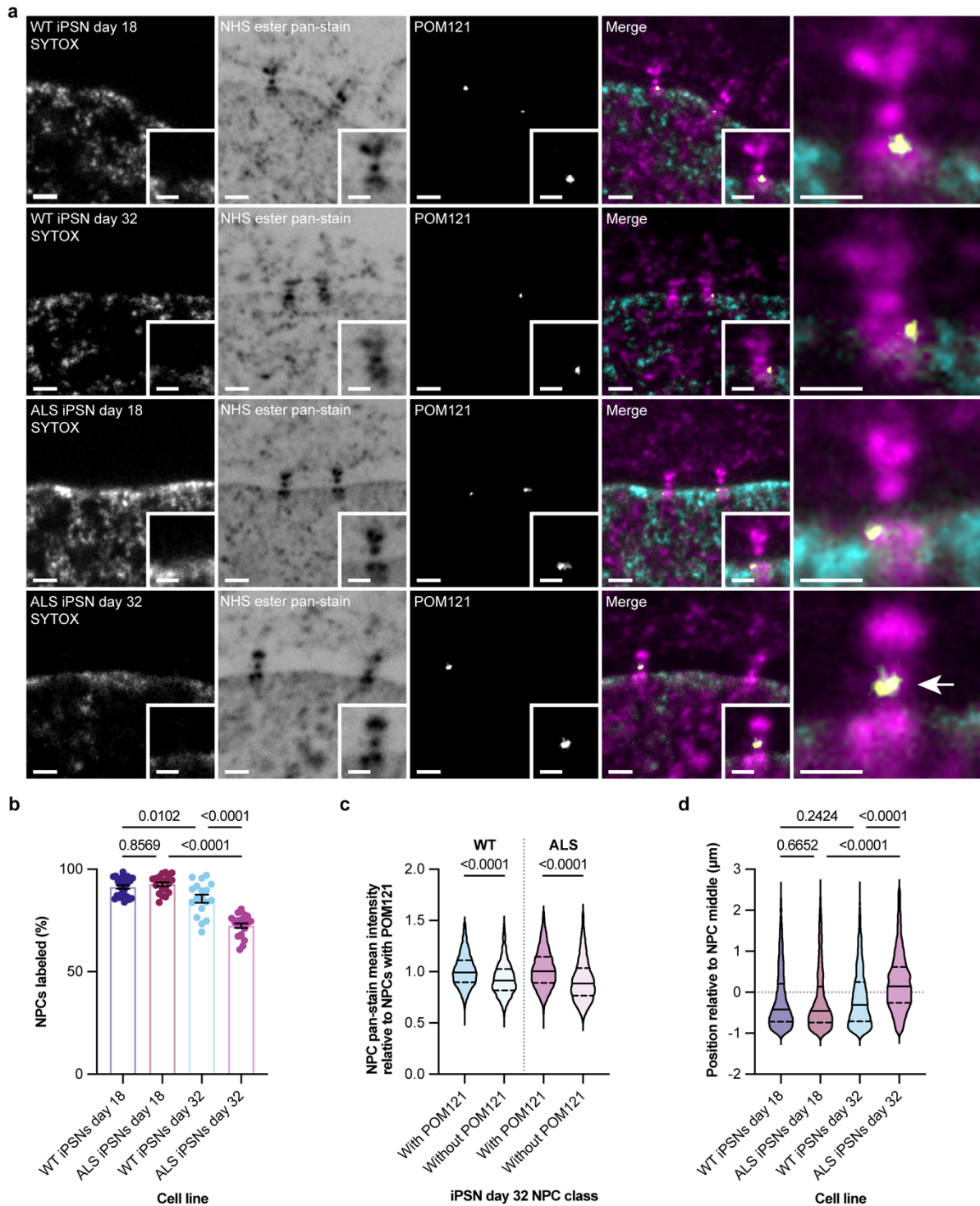
b. Nearly all segmented NPCs were immunostained with the POM121 antibody. Percentage of NPCs per nuclei labeled with an antibody against POM121 in the indicated cell line. Bars and error bars are the mean and s.d., respectively.

c. The bias in spatial distribution of POM121 staining at the nuclear ring is observed across the population of NPCs in all cell lines tested.

The NPC middle is denoted by the dotted line. Median values shown as solid lines and quartile values shown as dashed lines.

n=13831 segmented POM121 spots in n=6 HeLa cells, n=2314 segmented POM121 spots in n=4 SH-SY5Y cells, n=5300 segmented POM121 spots in n=10 A549 cells.

Cells from 1-2 independently expanded samples per cell line.

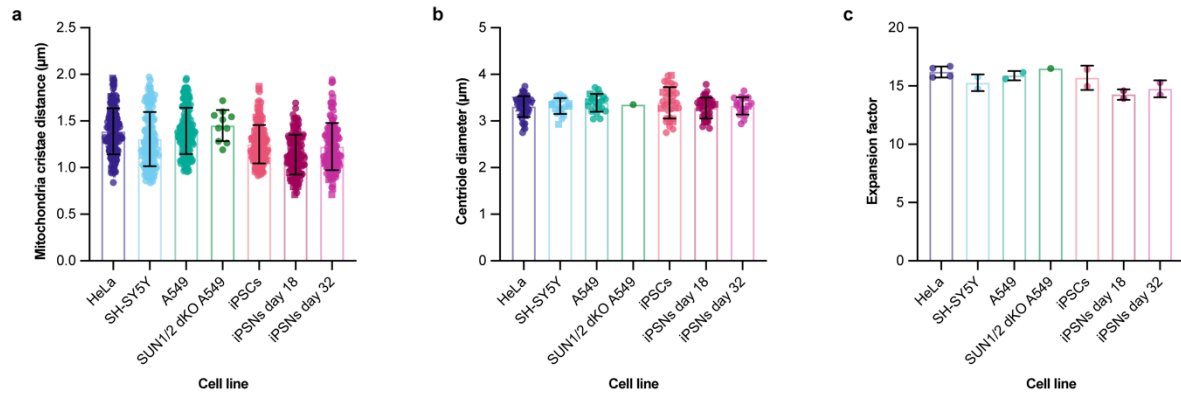


1

2 **Figure 7. POM121 shifts to the inner ring and is ultimately lost from NPCs in**
 3 **aged model ALS iPSCs**

4 **a.** POM121 is detected at the inner ring rather than the nuclear ring in “aged” model
 5 ALS iPSCs after 32 days of differentiation. Representative confocal fluorescence
 6 microscopy images of NPCs in expanded iPSCs derived from a patient with ALS or a
 7 matched WT control at indicated number of days after differentiation stained with

1 SYTOX, NHS ester pan-stain, and labeled with an antibody against POM121. Scale
2 bars 2 μm . Insets and far right panel show magnified views of the NPC, scale bars 1
3 μm . **b.** The fraction of NPCs labeled with POM121 antibody declines subtly over
4 days of differentiation in WT iPSNs but dramatically in ALS patient-derived iPSNs.
5 Percentage of NPCs per nuclei labeled with an antibody against POM121 in iPSNs
6 of the indicated genotype and number of days after differentiation. Bars and error
7 bars are the mean and s.d., respectively. n=82 cells from 2 independently expanded
8 samples per cell line. Ordinary one-way ANOVA with Tukey's multiple comparisons
9 test. **c.** NPCs lacking POM121 staining have reduced overall pan-stain signal
10 compared to POM121-positive NPCs in the same preparations. Quantification of
11 pan-stain mean intensity at segmented NPCs relative to segmented NPCs with
12 POM121 in iPSNs of the indicated genotype at day 32 post differentiation. n=7215
13 segmented NPCs in n=8 WT iPSNs day 18 cells, n=2005 segmented NPCs spots in
14 n=8 ALS iPSNs day 18 cells, n=9681 segmented NPCs in n=10 WT iPSNs day 32
15 cells, n=3146 segmented NPCs in n=10 ALS iPSNs day 32 cells. Each cell line was
16 expanded at the same time. Unpaired t test. **d.** Antibody staining of POM121 is
17 shifted from the nuclear ring to the inner ring across the population of POM121-
18 positive NPCs specifically in "aged" model ALS iPSNs. Spatial distribution of the
19 indicated genotype and number of days after differentiation relative to NPC middle
20 denoted by the dotted line. n=2492 segmented POM121 spots in n=4 WT iPSNs day
21 18 cells, n=1145 segmented POM121 spots in n=3 ALS iPSNs day 18 cells, n=1647
22 segmented POM121 spots in n=3 WT iPSNs day 32 cells, n=3093 segmented
23 POM121 spots in n=4 ALS iPSNs day 32 cells. Cells from 2 independently expanded
24 samples per cell line. Median values shown as solid lines and quartile values shown
25 as dashed lines. Kruskal-Wallis test with Dunn's multiple comparisons test.
26



d

Cell line	Expansion experiment	Average mitochondria cristae distance (µm)	Expansion factor assuming the average mitochondria cristae distance is 85 nm	Average centriole diameter (µm)	Expansion factor assuming the average centriole diameter is 210 nm	Average expansion factor
HeLa	1	1.46	17.22	3.39	16.16	16.69
	2	1.49	17.59	3.25	15.46	16.52
	3	1.36	15.99	3.30	15.72	15.86
	4	1.31	15.43	3.37	16.05	15.74
SH-SY5Y	1	1.20	14.16	3.23	15.37	14.76
	2	1.32	15.56	3.36	16.01	15.78
A549	1	1.27	14.94	3.42	16.28	15.61
	2	1.38	16.20	3.38	16.12	16.16
SUN1/2 dKO A549	1	1.45	17.08	3.35	15.94	16.51
iPSCs	1	1.18	13.94	3.40	16.19	15.06
	2	1.38	16.27	3.48	16.59	16.43
iPSNs day 18	1	1.16	13.69	3.25	15.47	14.58
	2	1.02	12.04	3.33	15.84	13.94
iPSNs day 32	1	1.26	14.77	3.32	15.79	15.28
	2	1.07	12.53	3.35	15.97	14.25

1

2 **Supplementary Figure 1. Approach to define the Pan-ExM expansion factor**
 3 **estimation and correction for each sample**

4 **a.** Mitochondria cristae distance in expanded samples of the indicated cell lines.

5 n=181 mitochondria in n=31 HeLa cells, n=132 mitochondria in n=27 SH-SY5Y cells,

6 n=154 mitochondria in n=31 A549 cells, n=10 mitochondria in n=2 SUN1/2 dKO

7 A549 cells, n=144 mitochondria in n=30 iPSCs, n=125 mitochondria in n=25 iPSNs

8 day 18 and n=128 mitochondria in n=26 iPSNs day 32. **b.** Centriole diameter in

9 expanded samples of the indicated cell lines. n=50 centrioles in HeLa cells, n=20 in

10 centrioles in SH-SY5Y cells, n=22 centrioles in A549 cells, n=1 centriole in SUN1/2

11 dKO A549 cells, n=34 centrioles in iPSCs, n=37 centrioles in iPSNs day 18 and

12 n=18 centrioles in iPSNs day 32. Cells from 1-4 independently expanded samples

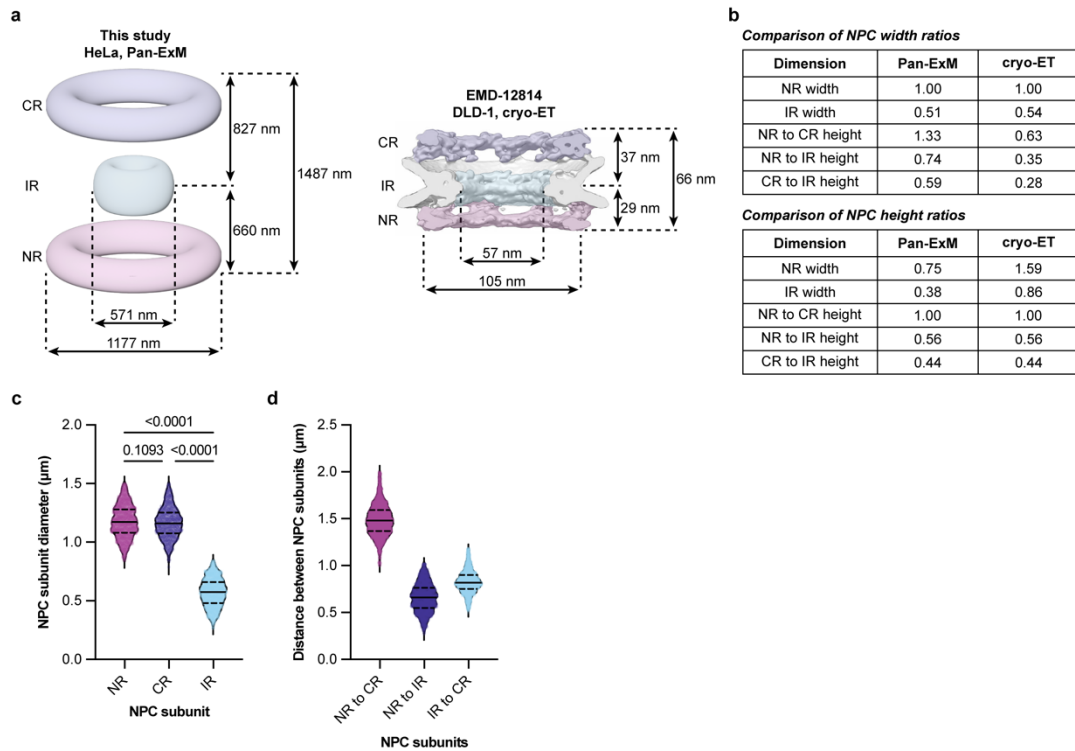
13 per cell line. **c.** Expansion factors are reproducible across cell lines and experiments.

14 Estimated expansion factors were determined by averaging mitochondrial cristae

15 distance and centriole diameter in cells expanded at the same time. n=15

16 independent expansion experiments. Bars and error bars are the mean and s.d.,

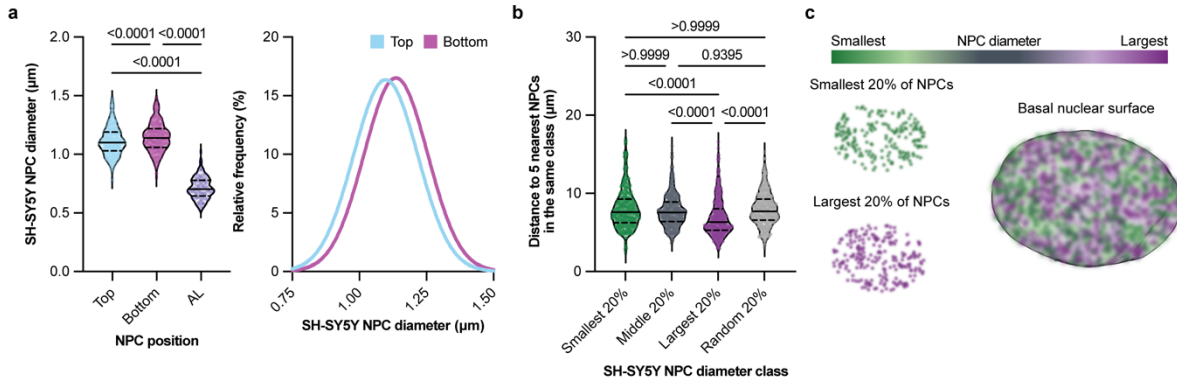
- 1 respectively. **d.** Summary of post-expansion measurements of cellular structures and
- 2 expansion factor calculations applied in this work.
- 3
- 4



1
2
3
4
5
6
7
8
9
10
11
12

Supplementary Figure 2. NPCs in Pan-ExM compared to cryo-ET

a. Average NPC dimensions in expanded samples compared to cryo-ET NPC density map. CR: cytoplasmic ring, IR: inner ring, NR: nuclear ring. **b.** Summary of NPC width and height ratio comparisons in Pan-ExM and cryo-ET samples. **c.** Diameter of the indicated NPC subunits in a Pan-ExM expanded HeLa cell. $n=1267$ segmented NRs, $n=1375$ segmented IRs. $n=802$ segmented CRs. Median values shown as solid lines and quartile values shown as dashed lines. Ordinary one-way ANOVA with Tukey's multiple comparisons test. **d.** Distance between NPC subunits in a Pan-ExM expanded HeLa cell $n=2061$ segmented NPCs.



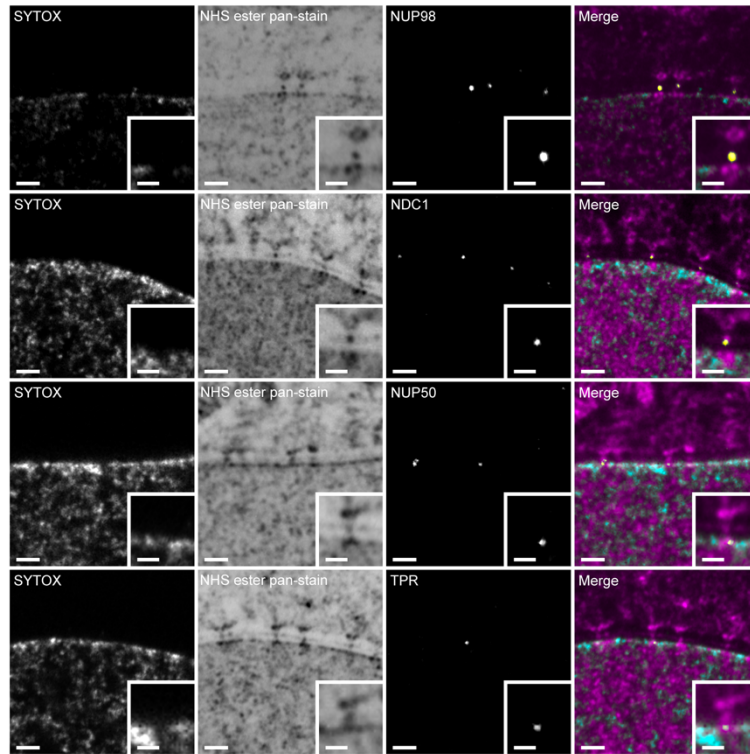
1

2 **Supplementary Figure 3. Local differences in NPC diameter are also observed**
3 **in SH-SY5Y cells**

4 **a, b.** The same trends in greater NPC dilation on the bottom of the nucleus (n=1403
5 NPCs in n=5 cells from a single expansion) and clustering of NPCs (n=1648) of like
6 diameter described in Figure 3 are also observed in SH-SY5Y cells. Median values
7 shown as solid lines and quartile values shown as dashed lines. Statistical tests:
8 ordinary one-way ANOVA with Tukey's multiple comparisons test (a) and Kruskal-
9 Wallis test with Dunn's multiple comparisons test (b). **c.** Visualization of NPCs at the
10 basal nuclear surface of an SH-SY5Y cell in (b) are color-coded according to NPC
11 diameter class. The smallest 20% of NPCs are shown in dark green, and the largest
12 20% are shown in dark purple. All NPCs are overlaid on a 3D rendering of the
13 nucleus.

14

15



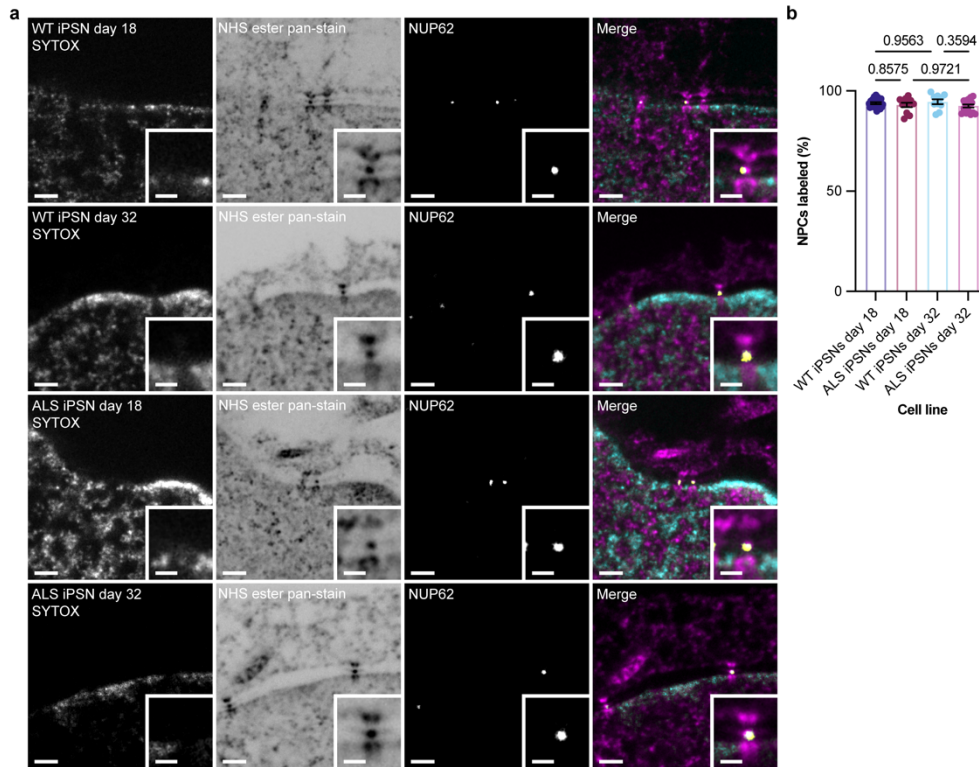
1

2 **Supplementary Figure 5. Additional nup antibody labeling to support ability of**
3 **Pan-ExM to reveal Nup position within the NPC ultrastructure**

4 Representative confocal fluorescence images of NPCs in expanded HeLa cells
5 stained with SYTOX, NHS ester pan-stain, and labeled with antibodies against the
6 indicated nups. Scale bars 2 μm . Insets show a magnified view of the NPC, scale
7 bars 1 μm .

8

9



1

2 **Supplementary Figure 6. Nup62 is retained and its position is unaffected in**
3 **aged model ALS iPSNs**

4 **a.** Representative confocal fluorescence microscopy images of NPCs in expanded
5 iPSNs derived from a patient with ALS or a matched WT control at indicated number
6 of days after differentiation stained with SYTOX, NHS ester pan-stain, and labeled
7 with an antibody against NUP62. Scale bars 2 μm. Insets show a magnified view of
8 the NPC, scale bars 1 μm. **b.** Percentage of NPCs per nuclei labeled with an
9 antibody against NUP62 in iPSNs of the indicated genotype and number of days
10 after differentiation. Bars and error bars are the mean and s.d., respectively. n=57
11 cells from 2 independently expanded samples per cell line. Ordinary one-way
12 ANOVA with Tukey's multiple comparisons test.

13

14

1 References

- 2
- 3 Akey, C.W., I. Echeverria, C. Ouch, I. Nudelman, Y. Shi, J. Wang, B.T. Chait, A. Sali, J.
4 Fernandez-Martinez, and M.P. Rout. 2023. Implications of a multiscale structure
5 of the yeast nuclear pore complex. *Mol Cell*. 83:3283-3302 e3285.
- 6 Akey, C.W., D. Singh, C. Ouch, I. Echeverria, I. Nudelman, J.M. Varberg, Z. Yu, F. Fang,
7 Y. Shi, J. Wang, D. Salzberg, K. Song, C. Xu, J.C. Gumbart, S. Suslov, J. Unruh,
8 S.L. Jaspersen, B.T. Chait, A. Sali, J. Fernandez-Martinez, S.J. Ludtke, E. Villa,
9 and M.P. Rout. 2022. Comprehensive structure and functional adaptations of
10 the yeast nuclear pore complex. *Cell*. 185:361-378.e325.
- 11 Arzt, M., J. Deschamps, C. Schmied, T. Pietzsch, D. Schmidt, P. Tomancak, R. Haase,
12 and F. Jug. 2022. LABKIT: Labeling and Segmentation Toolkit for Big Image Data.
13 *Frontiers in Computer Science*. 4.
- 14 Baskerville, V., S. Rapuri, E. Mehlhop, and A.N. Coyne. 2024. SUN1 facilitates CHMP7
15 nuclear influx and injury cascades in sporadic amyotrophic lateral sclerosis.
16 *Brain*. 147:109-121.
- 17 Bensidoun, P., T. Reiter, B. Montpetit, D. Zenklusen, and M. Oeffinger. 2022. Nuclear
18 mRNA metabolism drives selective basket assembly on a subset of nuclear pore
19 complexes in budding yeast. *Mol Cell*. 82:3856-3871.e3856.
- 20 Bley, C.J., S. Nie, G.W. Mobbs, S. Petrovic, A.T. Gres, X. Liu, S. Mukherjee, S. Harvey,
21 F.M. Huber, D.H. Lin, B. Brown, A.W. Tang, E.J. Rundlet, A.R. Correia, S. Chen,
22 S.G. Regmi, T.A. Stevens, C.A. Jette, M. Dasso, A. Patke, A.F. Palazzo, A.A.
23 Kossiakoff, and A. Hoelz. 2022. Architecture of the cytoplasmic face of the
24 nuclear pore. *Science*. 376:eabm9129.
- 25 Bui, K.H., A. von Appen, A.L. DiGuilio, A. Ori, L. Sparks, M.T. Mackmull, T. Bock, W.
26 Hagen, A. Andres-Pons, J.S. Glavy, and M. Beck. 2013. Integrated structural
27 analysis of the human nuclear pore complex scaffold. *Cell*. 155:1233-1243.
- 28 Carley, E., R.M. Stewart, A. Ziemann, I. Jalilian, D.E. King, A. Zubek, S. Lin, V. Horsley, and
29 M.C. King. 2021. The LINC complex transmits integrin-dependent tension to the
30 nuclear lamina and represses epidermal differentiation. *Elife*. 10.
- 31 Chandra, S., and C.P. Lusk. 2022. Emerging Connections between Nuclear Pore
32 Complex Homeostasis and ALS. *Int J Mol Sci*. 23.
- 33 Chang, W., H.J. Worman, and G.G. Gundersen. 2015. Accessorizing and anchoring the
34 LINC complex for multifunctionality. *J Cell Biol*. 208:11-22.
- 35 Cho, U.H., and M.W. Hetzer. 2020. Nuclear Periphery Takes Center Stage: The Role of
36 Nuclear Pore Complexes in Cell Identity and Aging. *Neuron*. 106:899-911.
- 37 Cordes, V.C., S. Reidenbach, and W.W. Franke. 1996. Cytoplasmic annulate lamellae
38 in cultured cells: composition, distribution, and mitotic behavior. *Cell Tissue
39 Res*. 284:177-191.
- 40 Coyne, A.N., V. Baskerville, B.L. Zaepfel, D.W. Dickson, F. Rigo, F. Bennett, C.P. Lusk,
41 and J.D. Rothstein. 2021. Nuclear accumulation of CHMP7 initiates nuclear pore
42 complex injury and subsequent TDP-43 dysfunction in sporadic and familial ALS.
43 *Sci Transl Med*. 13.
- 44 Coyne, A.N., and J.D. Rothstein. 2021. Nuclear lamina invaginations are not a
45 pathological feature of C9orf72 ALS/FTD. *Acta Neuropathol Commun*. 9:45.
- 46 Coyne, A.N., B.L. Zaepfel, L. Hayes, B. Fitchman, Y. Salzberg, E.C. Luo, K. Bowen, H.
47 Trost, S. Aigner, F. Rigo, G.W. Yeo, A. Harel, C.N. Svendsen, D. Sareen, and J.D.

- 1 Rothstein. 2020. G(4)C(2) Repeat RNA Initiates a POM121-Mediated Reduction
2 in Specific Nucleoporins in C9orf72 ALS/FTD. *Neuron*. 107:1124-1140.e1111.
- 3 Elosegui-Artola, A., I. Andreu, A.E.M. Beedle, A. Lezamiz, M. Uroz, A.J. Kosmalska, R.
4 Oria, J.Z. Kechagia, P. Rico-Lastres, A.L. Le Roux, C.M. Shanahan, X. Trepas, D.
5 Navajas, S. Garcia-Manyes, and P. Roca-Cusachs. 2017. Force Triggers YAP
6 Nuclear Entry by Regulating Transport across Nuclear Pores. *Cell*. 171:1397-
7 1410 e1314.
- 8 Feng, Q., M. Saladin, C. Wu, E. Cao, W. Zheng, A. Zhang, P. Bhardwaj, X. Li, Q. Shen,
9 L.E. Kapinos, M. Mariappan, C.P. Lusk, Y. Xiong, R.Y.H. Lim, and C. Lin. 2024.
10 Channel width modulates the permeability of DNA origami based nuclear pore
11 mimics. *bioRxiv*.
- 12 Fernandez-Martinez, J., and M.P. Rout. 2021. One Ring to Rule them All? Structural and
13 Functional Diversity in the Nuclear Pore Complex. *Trends Biochem Sci*. 46:595-
14 607.
- 15 Fontana, P., Y. Dong, X. Pi, A.B. Tong, C.W. Hecksel, L. Wang, T.-M. Fu, C. Bustamante,
16 and H. Wu. 2022. Structure of cytoplasmic ring of nuclear pore complex by
17 integrative cryo-EM and AlphaFold. *Science*. 376.
- 18 Freibaum, B.D., Y. Lu, R. Lopez-Gonzalez, N.C. Kim, S. Almeida, K.H. Lee, N. Badders,
19 M. Valentine, B.L. Miller, P.C. Wong, L. Petrucelli, H.J. Kim, F.B. Gao, and J.P.
20 Taylor. 2015. GGGGCC repeat expansion in C9orf72 compromises
21 nucleocytoplasmic transport. *Nature*. 525:129-133.
- 22 Funakoshi, T., M. Clever, A. Watanabe, and N. Imamoto. 2011. Localization of Pom121
23 to the inner nuclear membrane is required for an early step of interphase nuclear
24 pore complex assembly. *Mol Biol Cell*. 22:1058-1069.
- 25 Galy, V., O. Gadal, M. Fromont-Racine, A. Romano, A. Jacquier, and U. Nehrbass. 2004.
26 Nuclear retention of unspliced mRNAs in yeast is mediated by perinuclear Mlp1.
27 *Cell*. 116:63-73.
- 28 Hampoelz, B., M.T. Mackmull, P. Machado, P. Ronchi, K.H. Bui, N. Schieber, R.
29 Santarella-Mellwig, A. Necakov, A. Andrés-Pons, J.M. Philippe, T. Lecuit, Y.
30 Schwab, and M. Beck. 2016. Pre-assembled Nuclear Pores Insert into the
31 Nuclear Envelope during Early Development. *Cell*. 166:664-678.
- 32 Hampoelz, B., A. Schwarz, P. Ronchi, H. Bragulat-Teixidor, C. Tischer, I. Gaspar, A.
33 Ephrussi, Y. Schwab, and M. Beck. 2019. Nuclear Pores Assemble from
34 Nucleoporin Condensates During Oogenesis. *Cell*. 179:671-686 e617.
- 35 Hart, T., A.H.Y. Tong, K. Chan, J. Van Leeuwen, A. Seetharaman, M. Aregger, M.
36 Chandrashekhar, N. Hustedt, S. Seth, A. Noonan, A. Habsid, O. Sizova, L.
37 Nedyalkova, R. Climie, L. Tworzynski, K. Lawson, M.A. Sartori, S. Alibeh, D.
38 Tieu, S. Masud, P. Mero, A. Weiss, K.R. Brown, M. Usaj, M. Billmann, M. Rahman,
39 M. Constanzo, C.L. Myers, B.J. Andrews, C. Boone, D. Durocher, and J. Moffat.
40 2017. Evaluation and Design of Genome-Wide CRISPR/SpCas9 Knockout
41 Screens. *G3 (Bethesda)*. 7:2719-2727.
- 42 Huang, G., X. Zhan, C. Zeng, K. Liang, X. Zhu, Y. Zhao, P. Wang, Q. Wang, Q. Zhou, Q.
43 Tao, M. Liu, J. Lei, C. Yan, and Y. Shi. 2022a. Cryo-EM structure of the inner ring
44 from the *Xenopus laevis* nuclear pore complex. *Cell Res*. 32:451-460.
- 45 Huang, G., X. Zhan, C. Zeng, X. Zhu, K. Liang, Y. Zhao, P. Wang, Q. Wang, Q. Zhou, Q.
46 Tao, M. Liu, J. Lei, C. Yan, and Y. Shi. 2022b. Cryo-EM structure of the nuclear
47 ring from *Xenopus laevis* nuclear pore complex. *Cell Res*. 32:349-358.

- 1 Ihalainen, T.O., L. Aires, F.A. Herzog, R. Schwartlander, J. Moeller, and V. Vogel. 2015.
2 Differential basal-to-apical accessibility of lamin A/C epitopes in the nuclear
3 lamina regulated by changes in cytoskeletal tension. *Nat Mater.* 14:1252-1261.
- 4 Kessel, R.G. 1983. The structure and function of annulate lamellae: porous cytoplasmic
5 and intranuclear membranes. *Int Rev Cytol.* 82:181-303.
- 6 King, M.C., C.P. Lusk, and G. Blobel. 2006. Karyopherin-mediated import of integral
7 inner nuclear membrane proteins. *Nature.* 442:1003-1007.
- 8 Klughammer, N., A. Barth, M. Dekker, A. Fragasso, P.R. Onck, and C. Dekker. 2024.
9 Diameter dependence of transport through nuclear pore complex mimics
10 studied using optical nanopores. *Elife.* 12.
- 11 Kosinski, J., S. Mosalaganti, A. von Appen, R. Teimer, A.L. DiGuilio, W. Wan, K.H. Bui,
12 W.J. Hagen, J.A. Briggs, J.S. Glavy, E. Hurt, and M. Beck. 2016. Molecular
13 architecture of the inner ring scaffold of the human nuclear pore complex.
14 *Science.* 352:363-365.
- 15 Kozai, T., J. Fernandez-Martinez, T. van Eeuwen, P. Gallardo, L.E. Kapinos, A. Mazur, W.
16 Zhang, J. Tempkin, R. Panatala, M. Delgado-Izquierdo, B. Raveh, A. Sali, B.T.
17 Chait, L.M. Veenhoff, M.P. Rout, and R.Y.H. Lim. 2023. Dynamic molecular
18 mechanism of the nuclear pore complex permeability barrier. *bioRxiv.*
- 19 Krull, S., J. Dorries, B. Boysen, S. Reidenbach, L. Magnusius, H. Norder, J. Thyberg, and
20 V.C. Cordes. 2010. Protein Tpr is required for establishing nuclear pore-
21 associated zones of heterochromatin exclusion. *EMBO J.* 29:1659-1673.
- 22 Liu, Q., N. Pante, T. Misteli, M. Elsagga, M. Crisp, D. Hodzic, B. Burke, and K.J. Roux.
23 2007. Functional association of Sun1 with nuclear pore complexes. *J Cell Biol.*
24 178:785-798.
- 25 Lokareddy, R.K., R.A. Hapsari, M. van Rheenen, R.A. Pumroy, A. Bhardwaj, A. Steen,
26 L.M. Veenhoff, and G. Cingolani. 2015. Distinctive Properties of the Nuclear
27 Localization Signals of Inner Nuclear Membrane Proteins Heh1 and Heh2.
28 *Structure.* 23:1305-1316.
- 29 M'Saad, O., and J. Bewersdorf. 2020. Light microscopy of proteins in their
30 ultrastructural context. *Nat Commun.* 11:3850.
- 31 M'Saad, O., R. Kasula, I. Kondratiuk, P. Kidd, H. Falahati, J.E. Gentile, R.F. Niescier, K.
32 Watters, R.C. Sterner, S. Lee, X. Liu, P. De Camilli, J.E. Rothman, A.J. Koleske, T.
33 Biederer, and J. Bewersdorf. 2022. All-optical visualization of specific molecules
34 in the ultrastructural context of brain tissue. *bioRxiv.*
- 35 Megat, S., N. Mora, J. Sanogo, O. Roman, A. Catanese, N.O. Alami, A. Freischmidt, X.
36 Mingaj, H. De Calbiac, F. Muratet, S. Dirrig-Grosch, S. Dieterle, N. Van Bakel, K.
37 Müller, K. Sieverding, J. Weishaupt, P.M. Andersen, M. Weber, C. Neuwirth, M.
38 Margelisch, A. Sommacal, K.R. Van Eijk, J.H. Veldink, G. Lautrette, P. Couratier,
39 A. Camuzat, I. Le Ber, M. Grassano, A. Chio, T. Boeckers, A.C. Ludolph, F.
40 Roselli, D. Yilmazer-Hanke, S. Millecamps, E. Kabashi, E. Storkebaum, C. Sellier,
41 and L. Dupuis. 2023. Integrative genetic analysis illuminates ALS heritability and
42 identifies risk genes. *Nat Commun.* 14:342.
- 43 Mitchell, J.M., J. Mansfeld, J. Capitanio, U. Kutay, and R.W. Wozniak. 2010. Pom121
44 links two essential subcomplexes of the nuclear pore complex core to the
45 membrane. *J Cell Biol.* 191:505-521.
- 46 Mosalaganti, S., A. Obarska-Kosinska, M. Siggel, R. Taniguchi, B. Turonova, C.E.
47 Zimmerli, K. Buczak, F.H. Schmidt, E. Margiotta, M.T. Mackmull, W.J.H. Hagen,

- 1 G. Hummer, J. Kosinski, and M. Beck. 2022. AI-based structure prediction
2 empowers integrative structural analysis of human nuclear pores. *Science*.
3 376:eabm9506.
- 4 Nino, C.A., D. Guet, A. Gay, S. Brutus, F. Jourquin, S. Mendiratta, J. Salamero, V. Geli,
5 and C. Dargemont. 2016. Posttranslational marks control architectural and
6 functional plasticity of the nuclear pore complex basket. *J Cell Biol.* 212:167-
7 180.
- 8 Onischenko, E., E. Noor, J.S. Fischer, L. Gillet, M. Wojtynek, P. Vallotton, and K. Weis.
9 2020. Maturation Kinetics of a Multiprotein Complex Revealed by Metabolic
10 Labeling. *Cell.* 183:1785-1800 e1726.
- 11 Otsuka, S., A.M. Steyer, M. Schorb, J.K. Heriche, M.J. Hossain, S. Sethi, M. Kueblbeck,
12 Y. Schwab, M. Beck, and J. Ellenberg. 2018. Postmitotic nuclear pore assembly
13 proceeds by radial dilation of small membrane openings. *Nat Struct Mol Biol.*
14 25:21-28.
- 15 Otsuka, S., J.O.B. Tempkin, W. Zhang, A.Z. Politi, A. Rybina, M.J. Hossain, M. Kueblbeck,
16 A. Callegari, B. Koch, N.R. Morero, A. Sali, and J. Ellenberg. 2023. A quantitative
17 map of nuclear pore assembly reveals two distinct mechanisms. *Nature*.
18 613:575-581.
- 19 Ou, H.D., S. Phan, T.J. Deerinck, A. Thor, M.H. Ellisman, and C.C. O'Shea. 2017.
20 ChromEMT: Visualizing 3D chromatin structure and compaction in interphase
21 and mitotic cells. *Science.* 357.
- 22 Petrovic, S., D. Samanta, T. Perriches, C.J. Bley, K. Thierbach, B. Brown, S. Nie, G.W.
23 Mobbs, T.A. Stevens, X. Liu, G.P. Tomaleri, L. Schaus, and A. Hoelz. 2022.
24 Architecture of the linker-scaffold in the nuclear pore. *Science.* 376:eabm9798.
- 25 Rasala, B.A., C. Ramos, A. Harel, and D.J. Forbes. 2008. Capture of AT-rich chromatin
26 by ELYS recruits POM121 and NDC1 to initiate nuclear pore assembly. *Mol Biol*
27 *Cell.* 19:3982-3996.
- 28 Schermelleh, L., P.M. Carlton, S. Haase, L. Shao, L. Winoto, P. Kner, B. Burke, M.C.
29 Cardoso, D.A. Agard, M.G. Gustafsson, H. Leonhardt, and J.W. Sedat. 2008.
30 Subdiffraction multicolor imaging of the nuclear periphery with 3D structured
31 illumination microscopy. *Science.* 320:1332-1336.
- 32 Schindelin, J., I. Arganda-Carreras, E. Frise, V. Kaynig, M. Longair, T. Pietzsch, S.
33 Preibisch, C. Rueden, S. Saalfeld, B. Schmid, J.Y. Tinevez, D.J. White, V.
34 Hartenstein, K. Eliceiri, P. Tomancak, and A. Cardona. 2012. Fiji: an open-source
35 platform for biological-image analysis. *Nat Methods.* 9:676-682.
- 36 Schuller, A.P., M. Wojtynek, D. Mankus, M. Tatli, R. Kronenberg-Tenga, S.G. Regmi, P.V.
37 Dip, A.K.R. Lytton-Jean, E.J. Brignole, M. Dasso, K. Weis, O. Medalia, and T.U.
38 Schwartz. 2021. The cellular environment shapes the nuclear pore complex
39 architecture. *Nature.* 598:667-671.
- 40 Shen, W., B. Gong, C. Xing, L. Zhang, J. Sun, Y. Chen, C. Yang, L. Yan, L. Chen, L. Yao, G.
41 Li, H. Deng, X. Wu, and A. Meng. 2022. Comprehensive maturity of nuclear pore
42 complexes regulates zygotic genome activation. *Cell.* 185:4954-4970 e4920.
- 43 Singh, D., N. Soni, J. Hutchings, I. Echeverria, F. Shaikh, M. Duquette, S. Suslov, Z. Li, T.
44 van Eeuwen, K. Molloy, Y. Shi, J. Wang, Q. Guo, B.T. Chait, J. Fernandez-
45 Martinez, M.P. Rout, A. Sali, and E. Villa. 2024. The molecular architecture of the
46 nuclear basket. *Cell.*

- 1 Sirtori, R., J.G. M, M.P. E, A. Collins, L. Donatelli, and C. Fallini. 2024. LINC complex
2 alterations are a key feature of sporadic and familial ALS/FTD. *Acta Neuropathol*
3 *Commun.* 12:69.
- 4 Talamas, J.A., and M.W. Hetzer. 2011. POM121 and Sun1 play a role in early steps of
5 interphase NPC assembly. *J Cell Biol.* 194:27-37.
- 6 von Appen, A., J. Kosinski, L. Sparks, A. Ori, A.L. DiGuilio, B. Vollmer, M.T. Mackmull, N.
7 Banterle, L. Parca, P. Kastritis, K. Buczak, S. Mosalaganti, W. Hagen, A. Andres-
8 Pons, E.A. Lemke, P. Bork, W. Antonin, J.S. Glavy, K.H. Bui, and M. Beck. 2015. In
9 situ structural analysis of the human nuclear pore complex. *Nature.* 526:140-
10 143.
- 11 Walther, T.C., P. Askjaer, M. Gentzel, A. Habermann, G. Griffiths, M. Wilm, I.W. Mattaj,
12 and M. Hetzer. 2003. RanGTP mediates nuclear pore complex assembly. *Nature.*
13 424:689-694.
- 14 Yavuz, S., R. Santarella-Mellwig, B. Koch, A. Jaedicke, I.W. Mattaj, and W. Antonin.
15 2010. NLS-mediated NPC functions of the nucleoporin Pom121. *FEBS Lett.*
16 584:3292-3298.
- 17 Zhu, X., G. Huang, C. Zeng, X. Zhan, K. Liang, Q. Xu, Y. Zhao, P. Wang, Q. Wang, Q.
18 Zhou, Q. Tao, M. Liu, J. Lei, C. Yan, and Y. Shi. 2022. Structure of the cytoplasmic
19 ring of the *Xenopus laevis* nuclear pore complex. *Science.* 376:eabl8280.
- 20 Zimmerli, C.E., M. Allegretti, V. Rantos, S.K. Goetz, A. Obarska-Kosinska, I. Zagoriy, A.
21 Halavatyi, G. Hummer, J. Mahamid, J. Kosinski, and M. Beck. 2021. Nuclear
22 pores dilate and constrict in cellulo. *Science.* 374:eabd9776.
23